

MASTER OF SCIENCE THESIS

Modeling of Dielectric-Barrier Discharge Actuator

Implementation, validation and generalization of an electrostatic model

A. Bouchmal

March 2011

Modeling of Dielectric-Barrier Discharge Actuator Implementation, validation and generalization of an electrostatic model

MASTER OF SCIENCE THESIS

For obtaining the degree of Master of Science in Aerospace Engineering at
Delft University of Technology

A. Bouchmal

March 2011



Delft University of Technology

Copyright © A. Bouchmal
All rights reserved.

DELFT UNIVERSITY OF TECHNOLOGY
DEPARTMENT OF
AERODYNAMICS

The undersigned hereby certify that they have read and recommend to the Faculty of Aerospace Engineering for acceptance a thesis entitled “**Modeling of Dielectric-Barrier Discharge Actuator**” by **A. Bouchmal** in partial fulfillment of the requirements for the degree of **Master of Science**.

Dated: March 2011

Board of Examiners:

Prof. dr. ir. drs. H. Bijl

dr.ir. L.L.M. Veldhuis

dr.ir. S.J. Hulshoff

dr.ir. A.H. van Zuijlen

M. Kotsonis M.Sc

Abstract

Currently, one of the most promising active flow control device is the Dielectric-Barrier Discharge (DBD) actuator. Therefore, Delft University of Technology seeks to construct a model of this plasma actuator for use with CFD. The advantages of having a plasma actuator model for CFD purposes is clear: It facilitates the prediction of flows over different configurations and flow properties of interest for aerospace purposes.

There are currently two groups of plasma actuator models: Simplified models and First-principles based models. Although the First-principles based models are more accurate than simplified models, they are more complex and therefore computationally intensive. Because this is the first attempt at Delft University of Technology for the implementation of a plasma actuator model, simplicity is an essential starting point. The simplified model of Suzen & Huang is simple, fast and easy to implement and is therefore the first model considered. The implementation is done in the commercial CFD-software Fluent, by using the User-Defined Scalar transport equations (UDS). Two separate UDSs are computed: one for the electric potential ϕ and one for the net charge density ρ_c . The code is verified by means of the Method of Manufactured Solutions. The code is validated by comparison with the results obtained from the model of Suzen & Huang. The electric potential field, net charge density field and the corresponding body force field proved, although with minor differences, to be accurately modeled. The resulting flow field in quiescent air was qualitatively correct, however differences were found in the results obtained by Suzen & Huang and the results of the current simulation.

Finally, an attempt is made to generalize the model of Suzen & Huang and to analyze its capability of accurately modeling experimentally obtained body force field for a different plasma actuator configuration. The measurements of Kotsonis et al are used as a benchmark and the net charge density field is extracted from the body force measurements by division by the electric field strength. Even though the correct boundary conditions are applied, the model of Suzen & Huang is not able to accurately model the charge density field and body force field. Specifically, the model is not able to compute the change in plasma volume as a function of the applied voltage. Furthermore, the relation between the integrated horizontal body force and the applied voltage does not agree with the relation of $U_{max} \propto f_{b,x} \propto V_{pp}^{7/2}$ found in literature. An explanation for this could lie in the assumption in the derivation of the model that $\varphi \ll T$. Literature states that this assumption is questionable. Therefore, usage of the plasma actuator model for different voltages will introduce an inaccuracy in the magnitude of the integrated horizontal body force and therefore in the maximum induced velocity.

I would like to thank my mother, my father and my wife for all the love and support

Contents

Abstract	v
Acknowledgements	vi
Contents	ix
List of Figures	x
List of Tables	xi
List of Symbols	xiii
1 Introduction	1
1.1 Introduction	1
1.2 Approach	3
2 Physics and modeling of plasma actuator	5
2.1 Introduction to plasma	5
2.2 Plasma actuator physics	5
2.2.1 Introduction	5
2.2.2 Debye shielding	6
2.2.3 Working principle	7
2.2.4 Time scales	9
2.2.5 Mechanical properties	9
2.3 Previous work on plasma actuator modeling	13
2.3.1 Simplified models	13
2.3.2 First-principles based models	16
2.4 Trade-off	19

3	Implementation of plasma actuator model	21
3.1	Suzen & Huang Plasma Actuator Model	21
3.1.1	Mathematical model	21
3.1.2	Boundary conditions	24
3.2	Code Implementation and Verification	27
3.2.1	Implementation in Fluent	27
3.2.2	Code Verification	28
3.2.3	Configuration and Numerical Set-up	32
3.3	Validation Electrostatic Model	33
3.3.1	Notes regarding Suzen & Huang simulations	33
3.3.2	Electric potential, charge density and body force	33
3.3.3	Quiescent flow simulation	35
3.3.4	Domain and Grid studies	37
4	Generalization of the Suzen & Huang model	39
4.1	Introduction	39
4.2	Benchmark experimental data	40
4.3	Extraction of charge density field from experimentally obtained body force field	41
4.4	Hypothesis 1: Gaussian distribution with linear changing σ and μ , Debye length constant	47
4.5	Hypothesis 1B: Gaussian distribution and zero for $0 \leq x \leq 1\text{mm}$ with linear changing σ and μ , Debye length constant	51
4.6	Hypothesis 2: Gaussian distribution and zero for $0 \leq x \leq 1\text{mm}$ with linear changing σ and μ and Debye length	53
4.7	Hypothesis 3: Gaussian curve fit distribution with constant Debye length	56
4.8	Analysis of the model of Suzen & Huang	60
4.9	Limitations and usage of the model of Suzen & Huang	61
5	Conclusions and Next steps	63
5.1	Conclusions	63
5.2	Next steps	64
A	User-Defined Functions implemented in Fluent	67
B	Gaussian coefficients for Hypothesis 3	71

List of Figures

1.1	Classification of flow control [9]	2
2.1	Schematic drawing of the asymmetric DBD plasma actuator	6
2.2	Schematic drawing of the charge build-up on the dielectric material surface during the first half cycle (negative exposed electrode) a) and second half cycle (negative exposed electrode) b) [5]	8
2.3	Discrepancy maximum induced velocity versus applied voltage	10
2.4	Mechanical effects of the plasma actuator on the flow field [17]	11
2.5	Light emission measurements during a voltage cycle [5]	12
2.6	Space-time lumped element circuit model principle [4]	14
2.7	Comparison of the linearized force model electric field lines and the original electric field lines	15
3.1	Incorrect body force direction	23
3.2	Boundary conditions and computational domain for Equations 3.14 and 4.4 [25]	24
3.3	Gaussian for different values of σ	25
3.4	Dimensional and non-dimensional variables [25]	25
3.5	Plot of $\phi(x, y)$ in the chosen domain	29
3.6	Plot of the Error vs. Cell width	31
3.7	Configuration dimensions used by Suzen & Huang	32
3.8	Grid used for validation of model of Suzen & Huang	32
3.9	Comparison electric potential field	34
3.10	Comparison charge density field	34
3.11	Comparison of normalized body force field	34
3.12	Profile of the body force f_b above left edge of encapsulated electrode	35
3.13	Body force vector field	35
3.14	Comparison of streamlines near electrodes for $0 \leq x \leq 50\text{mm}$ and $0 \leq y \leq 45\text{mm}$	36
3.15	Results domain and grid independence	38

4.1	Actuator configuration used by Kotsonis et al [15]	41
4.2	Comparison of normalized body force field	41
4.3	Interpolated horizontal electric field component E_x	42
4.4	Horizontal body force component $f_{b,x}$	43
4.5	Integrated horizontal body force f_x for various voltages and curve fit	43
4.6	Extracted charge density field ρ_c	44
4.7	Extracted charge density profile on the wall $\rho_{c,w}$	45
4.8	Maximum charge density $\rho_{c,max}$ against peak-to-peak voltage V_{pp}	45
4.9	Integral of experimentally measured $\rho_{c,w}$ and curve fit	46
4.10	Height of the plasma h_p as a function of input voltage	46
4.11	Comparison of experimental and modeled charge density fields for Hypothesis 1	48
4.12	Extracted charge density profile on the wall together with a Gaussian fit	48
4.13	Comparison of experimental and horizontal body force fields for Hypothesis 1	49
4.14	Integrated horizontal body force f_x for various voltages using Hypothesis 1	50
4.15	Comparison of experimental and modeled charge density fields for Hypothesis 1B	51
4.16	Comparison of experimental and modeled horizontal body force fields for Hypothesis 1B	52
4.17	Integrated horizontal body force f_x for various voltages using Hypothesis 1B	52
4.18	Comparison of experimental and modeled charge density fields for Hypothesis 2	54
4.19	Comparison of experimental and modeled horizontal body force fields for Hypothesis 2	54
4.20	Integrated horizontal body force f_x for various voltages using Hypothesis 2	55
4.21	Extracted charge density profile on the wall together with a Gaussian fit for $V_{pp} = 8kV$	56
4.22	Extracted charge density profile on the wall together with a Gaussian fit for $V_{pp} = 10kV$	57
4.23	Extracted charge density profile on the wall together with a Gaussian fit for $V_{pp} = 12kV$	57
4.24	Extracted charge density profile on the wall together with a Gaussian fit for $V_{pp} = 14kV$	57
4.25	Extracted charge density profile on the wall together with a Gaussian fit for $V_{pp} = 16kV$	58
4.26	Comparison of experimental and modeled charge density fields for Hypothesis 3	58
4.27	Comparison of experimental and modeled body force fields for Hypothesis 3	59
4.28	Integrated horizontal body force f_x for various voltages using Hypothesis 3	59

List of Tables

2.1	Time scales plasma actuator problem	9
3.1	Boundary conditions MMS procedure	30
3.2	Errors MMS simulations	30
3.3	Results of the domain independence study	37
3.4	Results grid of the independence study	37
4.1	Integrated horizontal body force f_x obtained by Kotsonis et al	42
4.2	Gaussian parameters used for a manual curve fit	47
4.3	Integrated horizontal body force for Hypothesis 1	49
4.4	Integrated horizontal body force for Hypothesis 1B	51
4.5	Parameters used in Hypothesis 2	53
4.6	Integrated horizontal body force for Hypothesis 2	55
B.1	Coefficients used for Gaussian curve fit Hypothesis 3	71

List of Symbols

Latin Symbols

\vec{f}_b	Body force vector	$[N/m^3]$
B	Magnetic induction	[Tesla]
D	Electric induction	$[C/m^2]$
d	Distance of separation between electrodes	[m]
$D_{i,e}$	Diffusion coefficient of specie	[-]
E	Electric field	$[N/C]$
e	Elementary charge $1.60217646 \cdot 10^{-19}C$	[C]
H	Magnetic field strength	$[A/m]$
J	Free electric current	$[A/m^2]$
k	Boltzmann constant	[-]
$K_{i,e}$	Thermal conductivity of specie	[-]
m	Mass of a particle	$[kg]$
n_0	Background plasma density	$[1/m^3]$
n_e	Electron density in the plasma	$[1/m^3]$
n_i	Ion density in the plasma	$[1/m^3]$
T	Temperature of the species	[K]
U	Horizontal component of the velocity vector	$[m/s]$
U_{max}	Maximum induced horizontal velocity component	$[m/s]$
f^Δ	Discrete solution function	[-]
f^{exact}	Exact solution function	[-]
$f_{b,x}$	Horizontal component of the body force vector	$[N/m^3]$
f_x	Integrated horizontal component of the body force	[N]
G	Gaussian distribution function	[-]

h_p	Height of the plasma	[m]
R	Destruction term	[-]
S	Source term	[-]
T'	Kinetic temperature $kT[\text{K}] = eT[\text{eV}]$	[eV]
$Torr$	Pressure unit 1 Torr=133.32 Pa	[Torr]
V_{app}	Applied voltage	[V]
V_{pp}	Applied peak-to-peak voltage $V_{pp} = 2V_{app}$	[V]

Greek Symbols

ϵ	Permittivity $\epsilon = \epsilon_0 \epsilon_r$	$[C^2/Nm^2]$
ϵ_0	Permittivity of free space $8.854 \cdot 10^{-12} C^2/Nm^2$	$[C^2/Nm^2]$
ϵ_r	Relative permittivity	[-]
Γ	Diffusion coefficient	[-]
λ_d	Debye length	[m]
μ	Location parameter for Gaussian distribution function	[-]
Φ	Total electric potential $\Phi = \phi + \varphi$	[V]
ϕ	Electric potential due to external electric field	[V]
ρ_c	Net charge density or charge density	$[C/m^3]$
$\rho_{c,max}$	Maximum value of the net charge density on the wall	$[C/m^3]$
$\rho_{c,wall}$	Net charge density on the wall	$[C/m^3]$
σ	Scale parameter for Gaussian distribution function	[-]
φ	Electric potential due to net charge density	[V]

Abbreviations

AC	Alternating Current
CFD	Computational Fluid Dynamics
DBD	Dielectric-Barrier Discharge
DSMC	Direct Simulation Monte-Carlo
H.O.T.	Higher Order Terms
MMS	Method of Manufactured Solutions
PDE	Partial Differential Equation
PIC	Particle-In-Cell
UDF	User-Defined Function
UDS	User-Defined Scalar

Introduction

1.1 Introduction

Historically, engineers have always tried to use the laws of physics in order to obtain a desirable effect for mankind. In the field of aerodynamics, nothing is different. Due to its significance both technologically as well as scientifically, engineers are continuously looking for a way to control the flow in all possible ways and configurations.

Gad-El-Hak states that flow control can be divided in Passive and Active flow control [9]. Passive flow control devices require no auxiliary power and no control-loop. Examples of Passive flow control are: application of zig-zag tapes and dimples on surfaces. An Active flow control device requires a certain amount of energy input and a control loop. Gad-El-Hak goes further by dividing Active flow control devices in either Predetermined or Reactive flow control devices. Predetermined flow control includes the application of a steady or unsteady energy input without looking at the particular state of the flow. The control-loop is therefore open. Reactive flow control makes use of a closed control-loop where the control action is changing due to measured flow variables. Furthermore, Reactive flow control can be split in Feedforward and Feedback control. In Feedforward control, the measured variable and controlled variable are different. In Feedback control, a controlled variable is measured and compared with a reference value which then results in an adaptation of the control device. See Figure 1.1 for an overview of the classification of flow control methods.

The last couple of years, research in the field of active flow control has grown rapidly. The most promising active flow control device is the Dielectric-Barrier Discharge (DBD) plasma actuator, from now on referred to as *plasma actuator*. The plasma actuator has become popular due to the following properties: Low weight, low power consumption, no moving parts and flexibility of use. It can be used as a Predetermined or a Reactive flow control device. The plasma actuator can be placed in the group of flow control methods that uses injection of momentum in the near-wall region.

In order to manipulate a free airflow, three main fields of flow control can be investigated [17]:

- Flow separation
- Laminar to turbulent flow transition

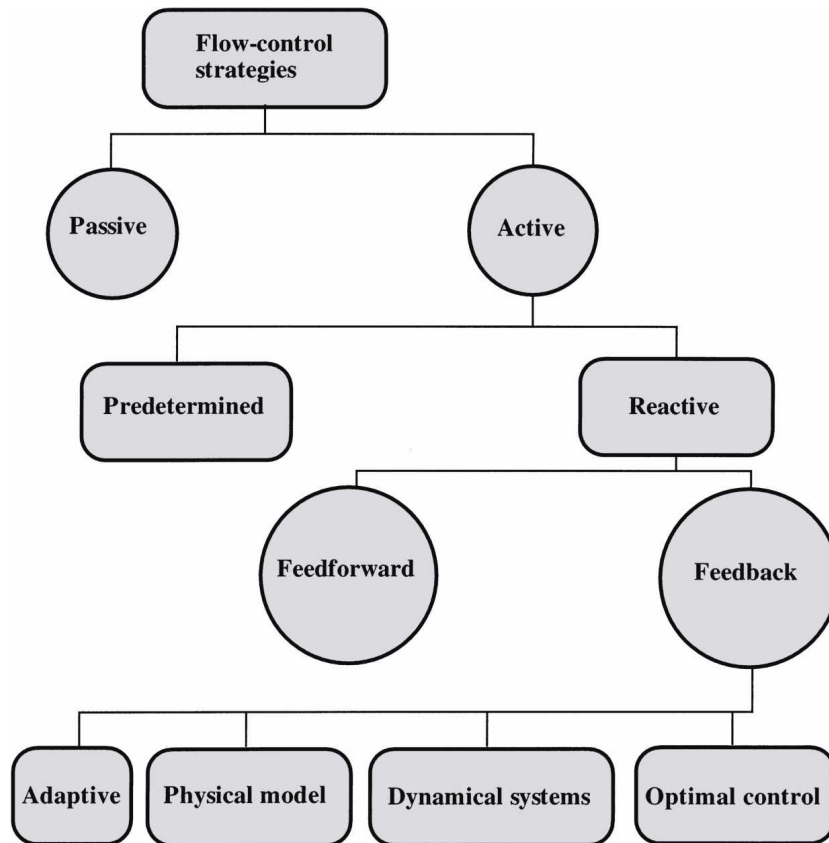


Figure 1.1: Classification of flow control [9]

- Turbulence

The plasma actuator has proven to be effective in these fields of flow control applications such as: exciting boundary layer instabilities on a sharp cone at Mach 3.5, lift augmentation on a wing section, low-pressure turbine blade separation control, unsteady vortex generation and airfoil leading-edge separation control [18].

Due to the limited momentum injection by the conventional plasma actuator, recently, nanosecond-pulsed plasma discharge mechanisms are proposed [16]. It has been shown that the effect of the plasma actuator on the flow field is much higher for nanosecond-pulsed plasma discharges. Experiments have shown high efficiency of the given mechanism to control boundary layer separation, lift and drag force coefficients, in addition to acoustic noise reduction in the Mach number range 0.05-0.85. The difference in physical mechanism of flow-discharge interaction is the main difference between the nanosecond-pulsed discharge and the AC discharge when applied to the plasma actuator. In the case of an AC discharge, the momentum transfer from the electric field to the gas and near-surface flow acceleration is the main mechanism of impact. For the nanosecond-pulsed discharge mechanism, the impact lies in the energy transfer to the near-surface gas and the fast heating of the layer [23].

Furthermore, the plasma actuator is proven to be successful in the delay of transition by means of Tollmien-Schlichting wave cancellation [10]. This technique aims at damping the instability waves while still at linear amplification stage. It is found, that the amplitude of the velocity fluctuations at the excitation frequency is reduced significantly depending on the distance from the wall.

1.2 Approach

In this work, we will start by analyzing different plasma actuator models described in literature. A suitable model will be chosen based on a set of requirements and the model will be programmed and implemented in CFD-software. After this, the model is verified and validated with experimental data. Finally, the applicability of the model in a different configuration and with different input parameters will be investigated. An attempt will be done to generalize the model in such a way that a wider field of application is achieved. A new approach will be used for this, where experimentally obtained body force fields are used to extract charge density fields of the plasma actuator model. These extracted charge density fields are then compared with the modeled charge density fields to give insight in the accuracy of the chosen model.

This work will contain the following objectives:

1. Comparison of different plasma actuator models
2. Selection of suitable plasma actuator model based on a set of requirements
3. Implementation of the chosen model in CFD-software
4. Verification and validation of the model
5. Research for generalization of the used model for a different configuration and input parameters

Physics and modeling of plasma actuator

2.1 Introduction to plasma

Plasma is by far the most common phase of matter in the universe. All the stars are made out of plasma and even the space surrounding them consists of plasma. It is common knowledge that a plasma is a gas which contains a certain concentration of ionized particles. Literature gives us the more precise following definition:

A plasma is a quasi-neutral gas of charged and neutral particles which exhibits collective behavior [3].

Charged particles are either electrons, positive ions or negative ions. If left to itself, a plasma exhibits a very strong tendency to become electrically neutral so that the charge density of ions and electrons is approximately equal. This is what is meant by *quasi-neutrality* [21]. With *collective behavior* is meant that there should be enough charged particles in the plasma present that it acts more or less as a continuum. Furthermore, plasmas can either be referred to as *hot* or *cold*. A hot plasma is a plasma which is almost fully ionized. In general one can say that the plasmas used in industrial applications are all *cold* plasmas which means that the only a small fraction of the gas is ionized.

2.2 Plasma actuator physics

2.2.1 Introduction

In literature, one can find dozens of different plasma actuator configurations [?]. The most common and widely used configuration is the asymmetric single DBD plasma actuator [?]. These consist of two electrodes that are separated by a dielectric material. One of the electrodes is exposed to air. The other electrode is completely encapsulated by a dielectric material. The electrodes are arranged in a asymmetrical way. The electrodes are connected to a high AC voltage power source. A schematic qualitative drawing of the asymmetric single DBD plasma actuator can be found in Figure 2.1.

Typically, a high AC voltage of 5 - 20kV is applied to the electrodes at frequencies ranging from 3-15 kHz. As a result, a cold plasma discharge appears on the dielectric material above the encapsulated

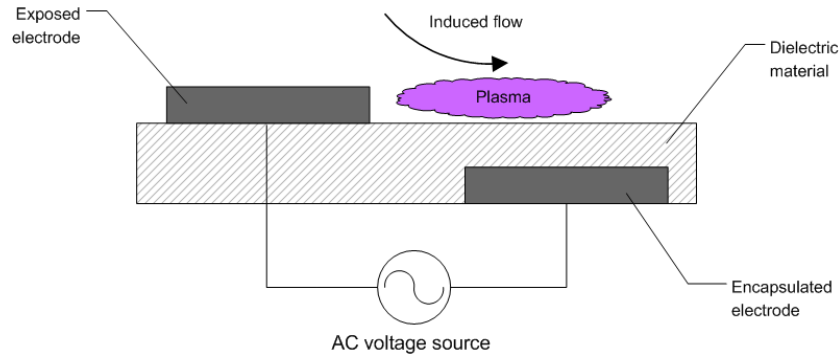


Figure 2.1: Schematic drawing of the asymmetric DBD plasma actuator

electrode. The plasma affects the flow by pumping momentum into the boundary layer region. We will elaborate on the working of the plasma actuator in the next section. This momentum addition can be used for flow control purposes, e.g. separation control.

2.2.2 Debye shielding

An important characteristic of plasma is the ability of the plasma to shield out electric potentials that are imposed on it. This concept could best be explained by a small example. Suppose we have a volume of plasma (a mixture of ions and electrons) and we insert two electrodes in the volume. One electrode will have a positive charge and the other a negative one. The electrodes will attract species of the opposite charge. Therefore a cloud of electrons will form around the positive electrode and a cloud of positive ions around the negative electrode. We will assume that the voltage source is strong enough to retain the potential on both the electrodes in spite of the clouds of opposite charge surrounding them. One can imagine that a certain specie which is on the edge of the cloud at a distance l from the electrode will be able to escape the attractive forces from the electrode due to the neutralizing surrounding cloud. This length l is known as the Debye length λ_d .

Literature tells us that the Debye length is given by [5]:

$$\lambda_d = \left(\frac{\varepsilon_0 k T_e}{n_0 e^2} + \frac{\varepsilon_0 k T_i}{n_0 e^2} \right)^{1/2} \quad (2.1)$$

in which n_0 is the background plasma density, k the Boltzmann constant, ε_0 is the permittivity of free space and T_i and T_e are respectively the temperature of a the ion and electron species. This equation can also be written in the following form [21]:

$$\lambda_d \approx 7434 \left(\frac{T'}{n_e} \right)^{1/2} \quad (2.2)$$

with $T' = kT/e$ being expressed in electron volts and the number density n_e in electrons per cubic meter. For plasmas used in industrial applications the kinetic temperature is approximately $eT' = 5eV$ and the number density is approximately n_e of 10^{16} particles/m³. This results in a Debye length of approximately $\lambda_d = 0.00017m$ [21]. Therefore, this value of $\lambda_d = 0.00017m$ is only indicative for industrial plasmas, however, and is not necessarily applicable to the DBD actuator case.

2.2.3 Working principle

Since we are dealing with an AC voltage source, there are two half-cycles. During the first half-cycle, the exposed electrode acts like an anode where the encapsulated electrode acts like a cathode. In the space between both electrodes, electrons are extracted from neutral particles by ionization. Under the electric field, these electrons are accelerated towards the anode and ionize the gas by collisions with neutral particles. The chemical reaction for the ionization is typically as follows:



where A is a neutral particle and A^+ a positive ion. From Equation 2.3, one can see that one electron colliding with one neutral particle results in two electrons and one charged particle. These two electrons collide with two neutral particles to form four electrons and so on. Therefore, an avalanche develops because the multiplication of electrons continues along their drift from the cathode to the anode. A discharge current is then created [17]. By definition, through the collisions momentum is transferred into the flow. It should be noted that the contribution of the electrons to the momentum transfer is small due to their low mass compared to the mass of the ions. The plasma is formed as the result of a series of discharges as electrons are transferred onto and off of the dielectric surface.

The charge build-up of the electrons on the dielectric material causes the plasma actuator to be self-limiting (in the case that the voltage is not continuously increased). In the first half-cycle, electrons drift from the exposed electrode (acting as a cathode) to the encapsulated electrode (acting as an anode) and accumulate on the surface of the dielectric. During the subsequent half-cycle these electrons return to the exposed electrode (which is now the anode). A schematic drawing of both half cycles can be seen in Figure 2.2. The plasma actuator induces a pulsed velocity with the same frequency as the AC voltage. However the induced velocity is higher during the negative half-cycle than the positive one. This will be demonstrated from experiments in Section 2.2.5.

The self-limiting effect of the plasma actuator, avoids the creation of an unfavorable so-called arc discharge. This arc discharge can have detrimental effects on the electronic equipment and causes the plasma actuator to become unstable. A glow discharge is the result of the self-limiting effect. The net effect of the plasma on the flow can be seen as a localized body force.

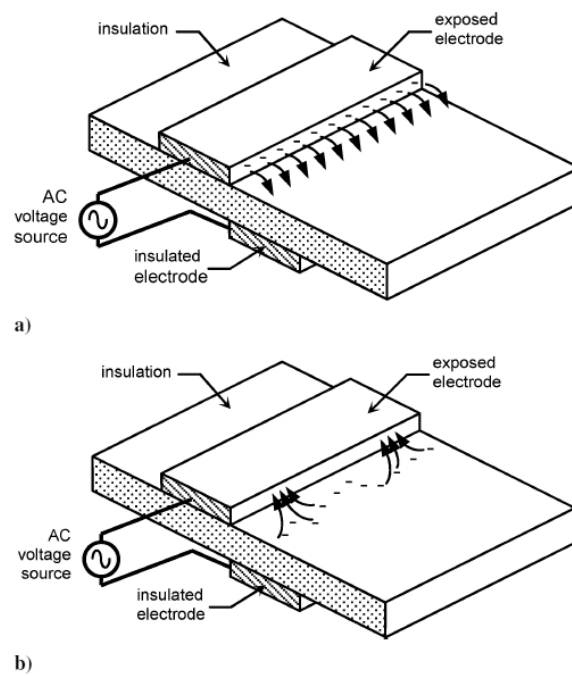


Figure 2.2: Schematic drawing of the charge build-up on the dielectric material surface during the first half cycle (negative exposed electrode) a) and second half cycle (negative exposed electrode) b) [5]

2.2.4 Time scales

The plasma is composed of charged particles. Still, the plasma is on average neutral since it is created by ionization of neutral fluid. The electrons will tend to move to the positive electrode, while the positive ions move to the negative electrode. This will result in an imbalance of charge within the plasma field. The charge imbalance will result in an electric field opposite to the electrodes' electric field. This so-called rearrangement process will continue until an equilibrium electric field is reached. The plasma formation consists of a number of different time scales. The first time scale in the plasma formation process, that of the rearrangement process, is in the order of 10^{-9} - 10^{-8} seconds (for an electron temperature of 1000- 10000K, with mobility velocity on the order of 10^5 - 10^6 m/s) [18].

The second time scale is given by the period of the half-cycle of the applied AC voltage. Assuming an AC frequency of 10kHz, the associated time scale is in the order of 10^{-4} seconds. This is approximately 10^4 times slower than the time scale of the rearrangement process.

The third time scale governs the response of the neutral flow on the plasma. This is in the order of 10^{-2} seconds. This is approximately 10^2 slower than the time scale of the AC voltage.

Summarizing, there are three different time scales in the plasma actuator modeling problem, see Table 2.1. If one is dealing with airflow, the four orders of magnitude difference in time scale justify the assumption that the formation of the plasma and the rearrangement process are instantaneous.

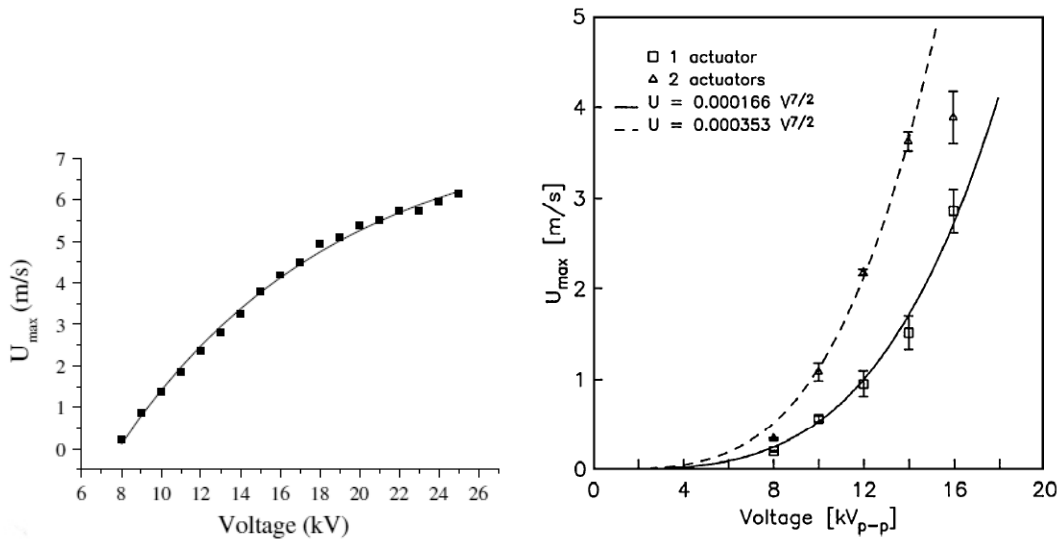
Process	Time scale [s]
Rearrangement process	10^{-9} - 10^{-8}
Frequency of voltage-source	10^{-4}
Response time fluid	10^{-2}

Table 2.1: Time scales plasma actuator problem

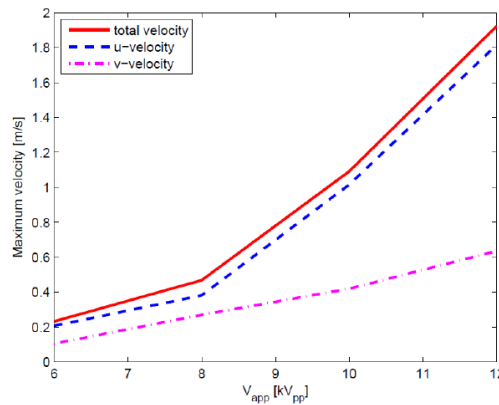
2.2.5 Mechanical properties

The effect of the plasma actuator on the induced flow field is a function of many parameters. For separation control purposed, especially the maximum induced velocity and the induced velocity profiles are interesting. In Figure 2.3, one can see the relation between the applied voltage and the maximum induced velocity found by different references. In the modeling of the plasma actuator this relation is very important. The correct form of this relation will broaden the field of applicability of the plasma actuator model. In Figure 2.3, the actuator configurations used in the references are different. Furthermore, the frequency and waveforms applied are different. Therefore a reasonable quantitative comparison is not possible. However we can tell something about whether or not there is a general proportionality between U_{max} and V_{pp} (a qualitative comparison). Note that the voltages used by Forte [8] are voltage amplitudes, while Enloe [5] uses peak-to-peak voltages (twice the voltage amplitude). Clearly, Forte et al 2.3(a) finds a different proportionality of U_{max} with respect to voltage than Enloe et al 2.3(b) and Kotsonis et al 2.3(c). The latter two correspond with each other with respect to the proportionality $U_{max} \propto V_{pp}^{7/2}$.

Forte found that for a single plasma actuator, the maximum induced ionic wind velocity is equal to 7 m/s at 0.5 mm distance from the wall [8]. For multiple plasma actuators, this maximum induced velocity is the amount of actuators placed multiplied by the maximum induced velocity per actuator [5]. One can see the influence of different parameters on the generated plasma in Figure



(a) Maximum induced velocity vs. voltage amplitude for a single plasma actuator with sine wave voltage for a single plasma actuator with triangular wave form 1kHz [8] (b) Maximum induced velocity vs. peak-to-peak voltage for a single plasma actuator with triangular wave form 5kHz [5]

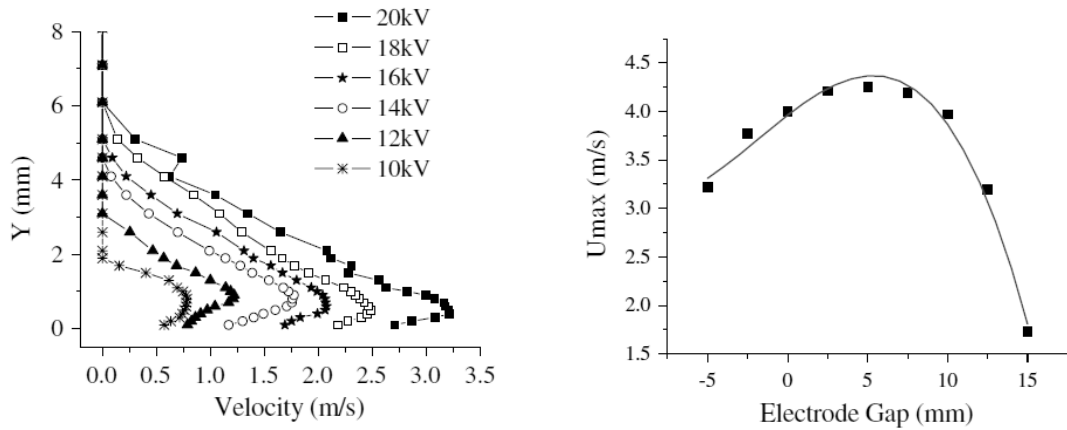


(c) Maximum induced velocity vs. peak-to-peak amplitude for a single plasma actuator with sine wave form 2kHz [14]

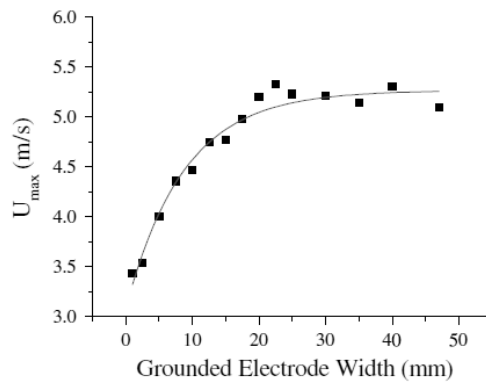
Figure 2.3: Discrepancy maximum induced velocity versus applied voltage

2.4. Figure 2.4(a) shows the change of the velocity profile for different voltage amplitudes. Figure 2.4(b) shows the maximum induced velocity with respect to electrode gap. Clearly, there seems to be a maximum electrode gap to obtain optimal velocity induction. Beyond this value of the electrode gap the induced velocity drops quickly. Figure 2.4(c) show the maximum induced velocity with respect to encapsulated electrode width. One can see that the maximum induced velocity increases asymptotically with increasing encapsulated electrode width.

In Figure 2.5, one can see the light emission measured from the plasma during a complete voltage cycle. The light emission is proportional to the plasma density. The plasma does not extend further than the downstream limit of the encapsulated electrode. Furthermore, the figure tells us that indeed during the negative half-cycle, the largest concentration of plasma is created.

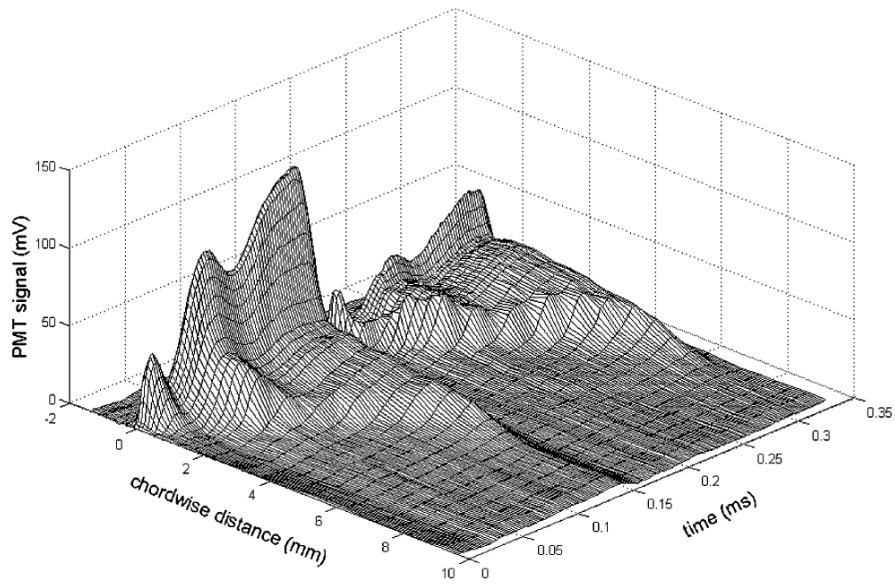


(a) Typical velocity profiles for different applied (b) Maximum induced velocity versus electrode gap voltages

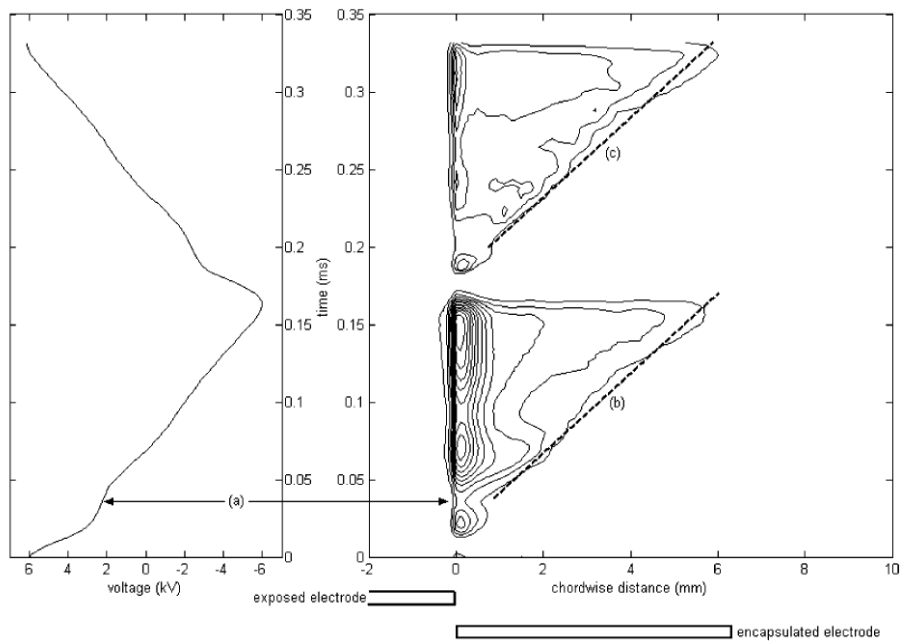


(c) Maximum induced velocity versus grounded electrode width

Figure 2.4: Mechanical effects of the plasma actuator on the flow field [17]



(a) 3D plot of light emission measurements during an AC voltage cycle



(b) Contours of light emission measurements during an AC voltage cycle

Figure 2.5: Light emission measurements during a voltage cycle [5]

2.3 Previous work on plasma actuator modeling

In the past, there are numerous plasma actuator models developed. Some successful, others less successful. In this section, we will describe some of the models. These models can be placed in two different categories: Simplified (phenomenological) models and First-principles based models. Simplified models use a reduction of complexity to describe the plasma. They are often based on phenomenological approaches of the physics. These type of models are discussed in Section 2.3.1. The First-principles based models use a more fundamental approach to model the physical mechanisms and these are discussed in Section 2.3.2. These models will be described briefly. For more detail, the reader is referred to the corresponding literature.

2.3.1 Simplified models

Electrostatic model

Suzen & Huang [25] used an electrostatic model with a Gaussian charge distribution to compute the plasma body force produced. Suzen & Huang proposed to split the electrostatic equations into two components: the first part due to the external electric field and the second part due to the electric field created by the charged particles. The main advantage of the model is its simplicity. This makes the model fast and easy to implement. Furthermore, the body force field can be decoupled from the flow field and can therefore be calculated prior to flow computations. Its drawbacks are its use of a time-independent plasma volume assumption and a voltage-independent charge density distribution function. A more elaborate description of the model is given in Section 3.1.

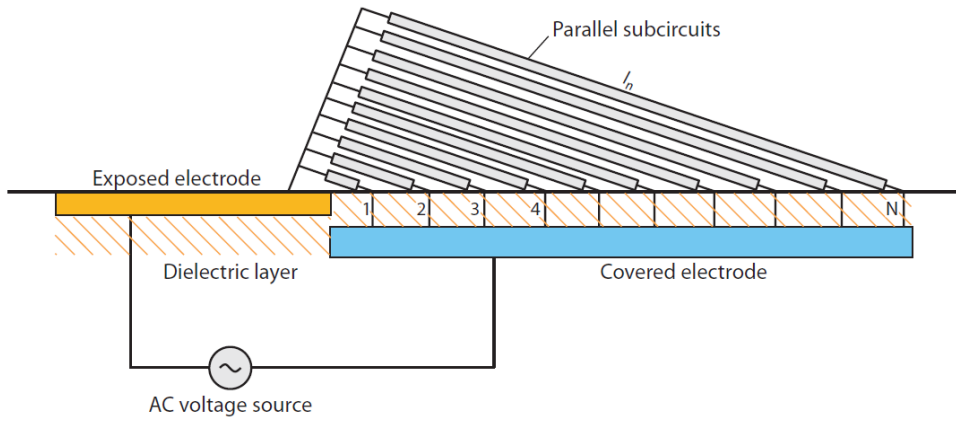
Lumped-element circuit model

A more complex electrostatic model is used by Orlov & Corke [19]: the Lumped element circuit model. Two physical electrodes make up the plasma actuator. Therefore it is modeled as a capacitor driven by the AC voltage. This is first suggested by Enloe [5]. Orlov & Corke modeled the plasma actuator by a network of lumped-element circuit elements, see Figure 2.6. The model consists of a number of capacitive elements and one resistive element which represents the plasma. Each of these elements are time-dependent, due to the changing plasma during the half-cycle of the applied AC voltage.

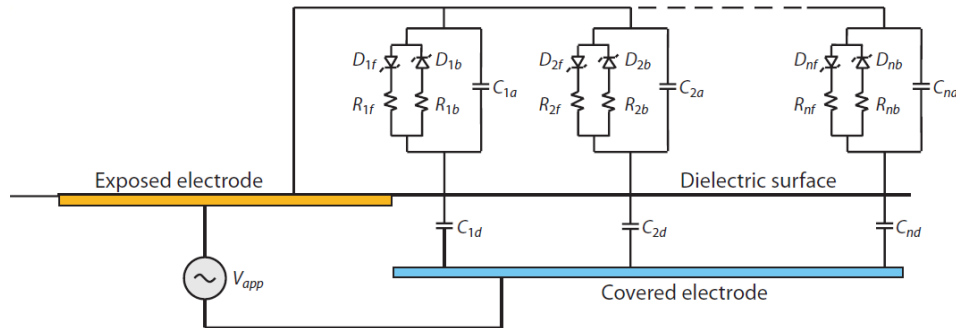
Orlov & Corke assume that the plasma is operating in a quasi-steady regime, when the charges are disturbed, so that they cancel the external electric field everywhere, except in the small regions near the electrodes. This allows them to make a quasi-DC assumption when modeling the plasma and computing the plasma body force. Using the Maxwell's equations they obtain a function for the body force per volume of plasma. The volume of the plasma is obtained by solving a set of five equations using the lumped element circuit model. One obtains the voltages at each node in the circuit and the physical movement of the plasma directly as a function of time. The lumped-element circuit model is successful in modeling the effect of the voltage on the body force. A shortcoming of the model is that it needs empirically determined coefficients which are functions of the frequency of the voltage. Therefore it is only valid for one single frequency.

Linearized force model

Jayaraman et al [13] use a simplification of the pattern of the electric field lines generated between the electrodes. One can see in Figure 2.7(a) that the electric field lines are concentrated at the



(a) Orlov & Corke [19] divide the region above the encapsulated electrode in N domains



(b) N domains are modeled using the parallel circuit arrangements

Figure 2.6: Space-time lumped element circuit model principle [4]

cathode and distributed over the anode. This lead to the assumption that the electric field lines could be modeled as being are parallel, except the small space near the cathode. This simplification linearized the field variation and therefore no detailed calculation of the electric field is needed.

The variation of the assumed electric field can be written as

$$|\vec{E}| = E_0 - k_1x - k_2y \tag{2.4}$$

in E_0 is the electric field on the dielectric material in the spacing between the electrodes and can be approximated as $E_0 = U/d$ where d is the distance of separation between the two electrodes in x -direction and U is the applied voltage. Furthermore k_1 and k_2 are positive constants. The sign of the two constants ensure that the electric field intensity decreases when one moves along the positive direction of the axes. In Figure 2.7 one can see a comparison between the actual electric field lines and the linearized field lines. Note that the line AB in Figure 2.7(b) is the plasma fluid boundary using linear approximation. The electric field strength outside this line is assumed not to be strong enough to ionize the air and therefore no plasma exists outside this line. This is defined by the breakdown voltage of the dielectric. The breakdown voltage is the minimum voltage needed, to induce electric conductivity of a portion of the dielectric.

The period of interest in a cycle is the time step Δt (the efficient half-cycle) during which the plasma discharge takes place and therefore the momentum is transfered into the flow. In Section 2.2.4 we found that the force is acting on the fluid in a quasi-steady way. Note that the force in the

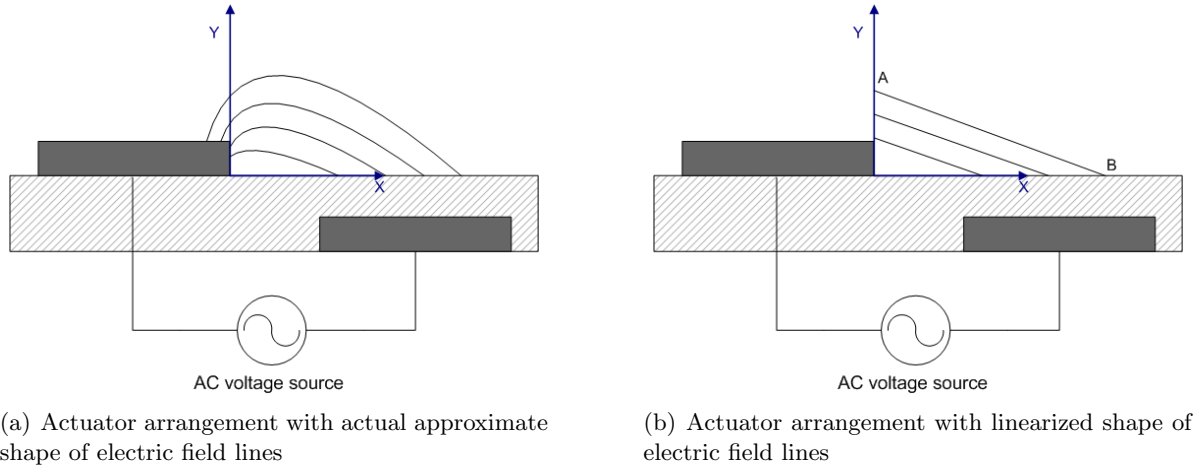


Figure 2.7: Comparison of the linearized force model electric field lines and the original electric field lines

subsequent half-cycle is neglected, since it has a negligible effect on the flow. Therefore the force can be time-averaged over the complete cycle:

$$F_x = \frac{\delta E_x \rho_c e_c \Delta t}{T_a} \quad (2.5)$$

$$F_y = \frac{\delta E_y \rho_c e_c \Delta t}{T_a} \quad (2.6)$$

with

$$E_x = \frac{Ek_2}{\sqrt{k_1^2 + k_2^2}} \quad (2.7)$$

$$E_y = \frac{Ek_1}{\sqrt{k_1^2 + k_2^2}} \quad (2.8)$$

$\delta = 1$ for $E < E_{cr}$ and $\delta = 0$ for $E \geq E_{cr}$. T_a is the period of the applied voltage cycle and e_c is the electronic charge. The equations for the body force (Equations 2.5 and 2.6) can directly be substituted as a source term in the Navier-Stokes equations. The largest drawback of this model is the harsh assumption that the electric field strength decreases linearly as one moves away from the inner edge of the electrode.

Potential flow model

Hall et al [11] used potential flow theory to model the effects of the plasma actuator. A simple model based on a doublet (source-sink) was developed to predict the effect of one particular actuator. By particular is meant a given actuator geometry and activating signal (i.e., fixed AC voltage amplitude, frequency and waveform) for which experimental data is available. This experimental data is used as closure to determine the doublet strength.

2.3.2 First-principles based models

Kinetic models

Kinetic models describe macroscopic properties of fluids by analyzing their molecular composition and motion. In general, kinetic models involve either solving the Boltzmann equation for the species velocity or the direct solution of particle models using e.g. Monte-Carlo methods. The Boltzmann equation is an equation for the distribution function $f(\bar{x}, \bar{v}, t)$ in a one-particle phase space, where \bar{x} is the position of the particle, \bar{v} is the velocity at time t :

$$\frac{\partial f}{\partial t} + \bar{v} \cdot \frac{\partial f}{\partial \bar{x}} + \frac{\bar{F}(\bar{x}, t)}{m} \cdot \frac{\partial f}{\partial \bar{v}} = \left(\frac{df}{dt} \right)_{coll} \quad (2.9)$$

$\bar{F}(\bar{x}, t)$ is the force field acting on the particles in the fluid and m is the mass of the particles. Only electromagnetic forces are considered, hence the force is proportional to the electric field and the charge. For electrons this is $\bar{F} = e \cdot \bar{E}$. The term on the right hand side of Equation 2.9 is the collision term and describes the collision between the particles. Equation 2.9 must be written for every type of charged species, i.e., electrons and ions. To obtain a self-consistent solution, one needs to solve for the electric field \bar{E} by using the Poisson equation:

$$\nabla \cdot \bar{E} = \frac{\rho}{\varepsilon_0} \quad (2.10)$$

where ρ is the charge density and ε_0 is the vacuum permittivity. The problem described above is multi-dimensional and time-dependent, which makes it, without any simplification or assumption, extremely difficult and time consuming to solve due to the short time scales of the electron and collision relaxation times.

The collision term in Equation 2.9 is the source of the non-linearity and is often modeled using a particle technique such as the Monte-Carlo method. The most common method is the Direct Simulation Monte-Carlo method (DSMC method). The DSMC method follows a large number of simulated particles simultaneously in order to reproduce the behavior of a large number of real atoms and molecules in the flow [2]. The fundamental assumption employed in the DSMC method is that the movement of the particles in a gas can be decoupled from the collisions between particles if a sufficiently small time step is used. Particle collisions are calculated using statistical collision models.

Alternatively, techniques such as the particle-in-cell (PIC) technique are used to model the collision term. This method is based on deterministic mechanics of particles in prescribed force fields. Particles are followed using a Lagrangian approach, whereas forces are computed simultaneously on an Eulerian stationary mesh. For the kinetic models one can say that the PIC technique is more deterministic while the Monte-Carlo technique is more statistical. A direct solution of the Boltzmann equation is also possible, however it is very time consuming.

Fluid models

When considering the kinetic models, one can ask whether all the information offered by the distribution function is needed. Since we are dealing with a distribution function f , it could be sufficient to obtain averages or moments of this function. In fluid models (or continuum models) moments are used to characterize distribution functions. The mathematical expression for the n^{th} moment of a distribution function about a value c is given by the following equation:

$$\mu'_n = \int_{-\infty}^{\infty} (x - c)^n f dx \quad (2.11)$$

with x being one of the quantities (e.g. velocity or a space coordinate). Due to the fact that the distribution function f is unknown, a method to compute the moments is required. There are three main methods to compute the moments:

- Assuming the form of the distribution function
- Expanding the distribution function in terms of basis functions
- Using phenomenological equations to describe integrals of the distribution function

Taking the first three moments of the Boltzmann equation together with Well's equation, one obtains the conservation equations [13]. The electron inertial terms are insignificant due to their negligible mass. For ions, at low pressure (< 100 mTorr) the inertial term is significant and for high pressure (≥ 1000 mTorr) the inertial term is insignificant.

Electrons

Continuity equation:

$$\frac{\partial n_e}{\partial t} + \nabla \cdot (n_e u_e) = n_e S - n_i n_e R \quad (2.12)$$

Momentum equation:

$$n_e \mu_e E - \nabla (n_e D_e) = n_e u_e \quad (2.13)$$

In most of the fluid models, the energy equation of the electrons is not solved.

Ions

Continuity equation:

$$\frac{\partial n_i}{\partial t} + \nabla \cdot (n_i u_i) = n_i S - n_i n_e R \quad (2.14)$$

Momentum equation:

$$n_i \mu_i E - \nabla(n_i D_i) = n_i u_i \quad (\text{High pressure discharge}) \quad (2.15)$$

$$n_i m_i \frac{\partial u_i}{\partial t} + n_i m_i (u_i \cdot \nabla) u_i + n_i m_i u_i N (K_{c,i} - K_{d,i}) + \nabla(n_i k T_i) - n_i q_i E = -n_i m_i u_i N K_{mi} \quad (2.16)$$

(Low pressure discharge)

In this case, there is no energy equation, because ions do not affect the ionization process. In numerical studies, the equations above are used together with the Poisson equation for the electric field:

$$\nabla \cdot E = \frac{e}{\varepsilon_0} \left(\sum n_i - n_e \right) \quad (2.17)$$

The parameters of the conservation equations can be obtained by solving the spatially homogeneous Boltzmann equation or from experimental data.

Hybrid models

To avoid computational heavy kinetic simulations and still not lose to much accuracy, hybrid models are used. These hybrid models treat some parts of the flow as a fluid and others kinetically. Belenguer et al [1] and Surendra et al [24] worked on a so-called bulk-beam model, which models the high-energy electrons as particles (beam) and other electrons and ions as a fluid (bulk). Fiala et al [7] used a fluid model where the ionization term is simulated using the Monte-Carlo method.

Comparison

Fluid models are a simplification of the kinetic models (considering only the first few moments). Kinetic models are more accurate for low pressures (<100 mTorr [13]). This is easily explained. If the pressure is relatively low, the assumption of the flow being a continuum fails and therefore the accuracy decreases. Furthermore, note that fluid models are impractical or inaccurate in situations where the deviations from equilibrium are strong, for example due to the presence of large gradients or strong transient effects. Computationally, kinetic models are much more intensive than fluid models (one order of magnitude longer running time) [13]. This is because fluid models deal with macroscopic quantities and being a simplification of the more complex kinetic models.

2.4 Trade-off

A trade-off has to be made to choose which plasma actuator model will be implemented. This is the first attempt to implement a plasma actuator model at the Faculty of Aerospace Engineering at Delft University of Technology. Therefore, one should start-off as simple as possible preferably with a time-averaged plasma actuator model. Because we are interested in the net effect of the plasma actuator on the flow field, we will use an electrostatic model which does not model the plasma build-up during the half-cycles of the applied AC voltage. This significantly simplifies the choice for the plasma actuator model because the First-principles based models are dropped. Although the first-principles based models are more accurate than simplified models, they are more complex and therefore computationally intensive.

This brings us at the simplified models. An interesting starting point for the implementation of a plasma actuator model is the model of Suzen & Huang. It is simple, fast and easy to implement. The method of implementation of the model of Suzen & Huang is discussed in the following chapter. Furthermore, the similarities between the model of Suzen & Huang and the lumped-element circuit model are considerable. Therefore a successful implementation of the model of Suzen & Huang can be used as a first step to implement the more accurate time-dependent lumped-element circuit model.

Implementation of plasma actuator model

In this chapter, the model of Suzen & Huang is elaborately described together with the used boundary conditions. Furthermore, the model is verified and validated with the results obtained by Suzen & Huang.

3.1 Suzen & Huang Plasma Actuator Model

3.1.1 Mathematical model

When imposing a high AC voltage on the arrangement of two electrodes separated by a dielectric layer, the air between the electrodes starts to ionize and plasma is formed. The plasma results in a body force that acts on the flow in either a steady or unsteady manner. Because we are dealing with plasmas, the equations of Maxwell are introduced (respectively Gauss law, Gauss law for magnetism, Faraday's law of induction and Ampere's circuital law):

$$\begin{aligned}\nabla \cdot \vec{D} &= \rho_c \\ \nabla \cdot \vec{B} &= 0 \\ \nabla \times \vec{E} &= -\frac{\partial \vec{B}}{\partial t} \\ \nabla \times \vec{H} &= \vec{J} - \frac{\partial \vec{D}}{\partial t}\end{aligned}\tag{3.1}$$

where \vec{H} is the magnetic field strength, \vec{B} is the magnetic induction, \vec{E} is the electric field strength, \vec{D} is the electric induction, \vec{J} is the electric current and ρ_c is the charge density. We assume that the charges in the plasma have sufficient amount of time for the redistribution process and the whole system is quasi-steady. These assumptions yield, the electric current, \vec{J} , the magnetic field, \vec{H} , and the magnetic induction, \vec{B} , are equal to zero, as well as the time derivatives of the electric induction, $\frac{\partial \vec{D}}{\partial t}$, and the magnetic induction, $\frac{\partial \vec{B}}{\partial t}$. This leaves two of the four Maxwell equations:

$$\begin{aligned}\nabla \cdot \vec{D} &= \rho_c \\ \nabla \times \vec{E} &= 0\end{aligned}\tag{3.2}$$

We use the relation between the electric induction and the electric field strength:

$$\vec{D} = \varepsilon \cdot \vec{E}\tag{3.3}$$

where $\varepsilon = \varepsilon_0 \varepsilon_r$, ε_0 is the permittivity of free space and ε_r is the relative permittivity. Equations 3.2 can then be written as:

$$\begin{aligned}\nabla \cdot \varepsilon \vec{E} &= \rho_c \\ \nabla \times \vec{E} &= 0\end{aligned}\tag{3.4}$$

Furthermore $\nabla \times \vec{E} = 0$ implies that the electric field can be derived from the gradient of a scalar potential Φ :

$$\vec{E} = -\nabla \Phi\tag{3.5}$$

Substitution of Equation 3.5 in Equation 3.4 yields:

$$\nabla \cdot (\varepsilon_r \nabla \Phi) = -\frac{\rho_c}{\varepsilon_0}\tag{3.6}$$

Now let us look at the electric potential due to the net charge density (Equation 4.3). Note that sometimes the net charge density is referred to simply as charge density. If we use the Boltzmann relation:

$$n_{i,e} = n_0 \exp\left(\frac{e\varphi}{k_b T}\right)\tag{3.7}$$

The following relation can be written:

$$\frac{\rho_c}{\varepsilon_0} = e(n_i - n_e) = -e \frac{n_0}{\varepsilon_0} \left[\exp\left(\frac{e\varphi}{kT_i}\right) + \exp\left(\frac{e\varphi}{kT_e}\right) \right]\tag{3.8}$$

with φ being the local electric potential. Expanding the exponential functions in a Taylor series for $\varphi \ll T$, Equation 3.8 becomes, to lowest order of φ/T :

$$\frac{\rho_c}{\varepsilon_0} \approx -e^2 \frac{n_0}{\varepsilon_0} \varphi \left[\left(\frac{1}{kT_i}\right) + \left(\frac{1}{kT_e}\right) \right]\tag{3.9}$$

Introduction of the Debye length (Equation 2.1) yields:

$$\rho_c = -\frac{\varepsilon_0}{\lambda_d^2} \Phi\tag{3.10}$$

The body force induced by the plasma actuator on the flow can be expressed by the Lorentz equation as (neglecting the magnetic forces)

$$\vec{f}_b = \rho_c \vec{E} \quad (3.11)$$

In Equation 3.11, \vec{f}_b is the body force per unit volume, ρ_c is the net charge density and \vec{E} is the electric field generated by the electrodes. Substitution of Equation 3.10 in Equation 3.11 yields:

$$\vec{f}_b = -\frac{\varepsilon_0}{\lambda_d^2} \Phi \cdot \vec{E} \quad (3.12)$$

Analysis of Equation 3.11 shows that independent of which electrode the voltage is applied to (Case I or Case II), the body force is always directed from encapsulated electrode to the exposed electrode, see Figure 3.1. It is known that the body force, must be directed in the opposite direction.

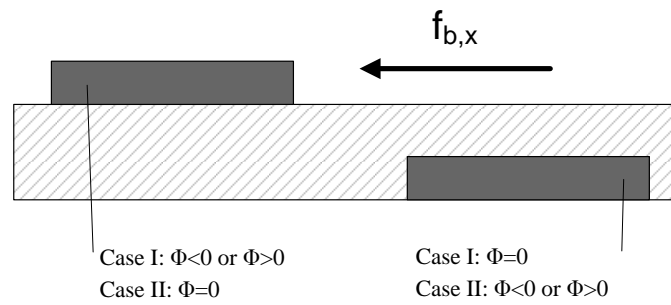


Figure 3.1: Incorrect body force direction

To obtain the correct direction, the potential Φ is decomposed in two parts: the potential due to the external electric field ϕ and the potential due to the net charge density φ :

$$\Phi = \phi + \varphi \quad (3.13)$$

Assuming that the Debye length is small and the charge on the wall above the encapsulated electrode is small, the distribution of charged particles in the domain is governed by the potential due to the electric charge on the wall and is unaffected by the external electric field. Note that the grid spacing should not be larger than the Debye length. It is possible to write two independent equations of the two potentials. For the potential due to the external electric field, the following Poisson equation is found:

$$\nabla \cdot (\varepsilon_r \nabla \phi) = 0 \quad (3.14)$$

For the potential due to the net charge density, the following Helmholtz equation is found:

$$\nabla \cdot (\varepsilon_r \nabla \varphi) = -\frac{\rho_c}{\varepsilon_0} \quad (3.15)$$

Using Equation 3.10, Equation 3.15 can be written as:

$$\nabla \cdot (\varepsilon_r \nabla \rho_c) = \frac{\rho_c}{\lambda_d^2} \quad (3.16)$$

Equations 3.14 and 4.4 yield respectively the variable ϕ and ρ_c . In order to obtain the correct direction of the induced body force, the net charge density ρ_c is synchronized with the applied voltage. The body force per unit volume is obtained as follows:

$$\vec{f}_b = \rho_c \vec{E} = \rho_c (-\nabla \phi) \quad (3.17)$$

The body force obtained from equation 3.17 can directly be implemented in the Navier Stokes equations as a source term.

3.1.2 Boundary conditions

Because there are two different equations that need to be solved (Equations 3.14 and 4.4), the computational domain has two different sets of boundary conditions for these equations. The applied AC voltage at the exposed electrode is given by:

$$\phi(t) = \phi^{\max} f(t) \quad (3.18)$$

The wave form function $f(t)$ can e.g. be a sine wave given by:

$$f(t) = \sin(2\pi\omega t) \quad (3.19)$$

where ω is the frequency and ϕ^{\max} is the amplitude. The wave form function $f(t)$ is a time-dependent boundary condition and can be used to model both steady and unsteady (duty cycles) actuator arrangements. For the steady case, $f(t)$ can be set to be a square wave. For unsteady cases, different frequencies and wave forms can be used to simulate actuation with different duty cycles.

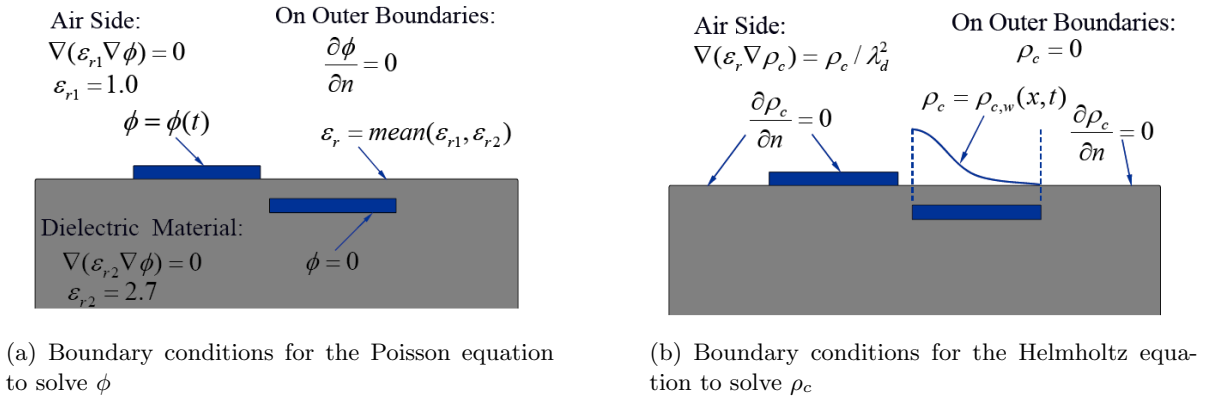


Figure 3.2: Boundary conditions and computational domain for Equations 3.14 and 4.4 [25]

Furthermore, for the net charge density boundary condition applied on the wall above the encapsulated electrode is given by:

$$\rho_{c,w}(x,t) = \rho_c^{\max} G(x) f(t) \quad (3.20)$$

From light intensity measurements, it is known that the net charge density distribution can be modeled by a half Gaussian distribution $G(x)$ [5][6]. This is given by:

$$G(x) = \exp\left[\frac{-(x - \mu)^2}{2\sigma^2}\right] \quad (3.21)$$

In the simulation, the parameters μ and σ are set such that the peak charge density corresponds to the left edge of the encapsulated electrode and to obtain a gradual decay of the charge density from the left to the right edge of the electrode (see Figure 3.3). Suzen & Huang chose a value of $\sigma/L = 0.3$ and μ depends on the chosen frame of reference and L being equal to the encapsulated electrode width.

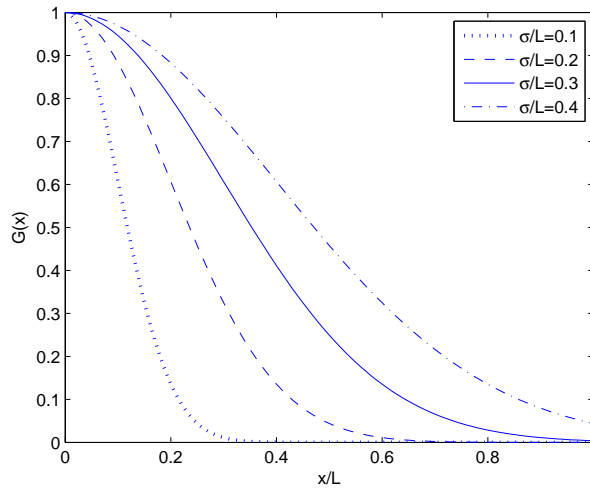


Figure 3.3: Gaussian for different values of σ

To obtain a fully decoupled problem, non-dimensional variables are introduced. This allows the computation of the solutions of Equations 3.14 and 4.4 only once at the beginning of the computation. With these solutions it is possible to calculate the electric potential and the net charge density at any given time with any amplitude by transformation to dimensional variables. The non-dimensional boundary conditions are shown in Figure 3.4.

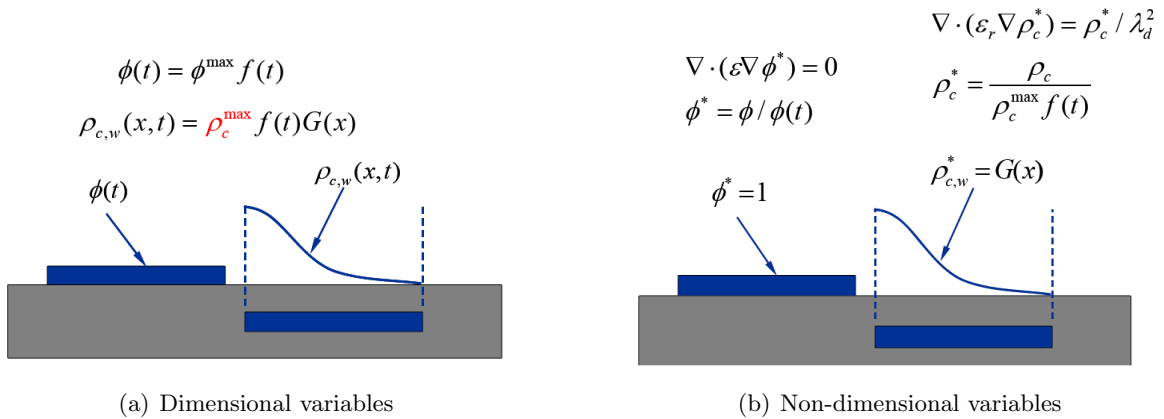


Figure 3.4: Dimensional and non-dimensional variables [25]

The parameters that need to be calibrated are λ_d and ρ_c^{\max} . For industrial plasmas under consideration, we found that $\lambda_d \approx 0.00017\text{m}$. Suzen & Huang obtain the following calibrated parameters:

$\lambda_d = 0.001\text{m}$ and $\rho_c^{\text{max}} = 0.0008\text{C}/\text{m}^3$. These are calibrated by Suzen & Huang for the model validation with the experimental results done by Jacob et al [12].

3.2 Code Implementation and Verification

The following section deals with the implementation of the model of Suzen & Huang in Fluent. Furthermore, the numerical set-up is discussed. Finally, the implemented code is verified using the Method of Manufactured Solutions (MMS).

3.2.1 Implementation in Fluent

To implement the model of Suzen & Huang in Fluent, use is made of the so-called User-Defined Scalar (UDS) Transport Equations. Fluent allows the definition of a UDS transport equation by setting the parameters of the following equation:

$$\underbrace{\frac{\partial \phi}{\partial t}}_{Unsteady} + \frac{\partial}{\partial x_i} \left[\underbrace{F_i \phi}_{Convection} - \Gamma \underbrace{\frac{\partial \phi}{\partial x_i}}_{Diffusion} \right] = \underbrace{S_\phi}_{Sources} \quad (3.22)$$

ϕ is the solved scalar quantity and Γ is the diffusion coefficient. Since we are dealing with a steady-state and we set the convective term equal to zero, Equation 3.22 can be written as:

$$\nabla \cdot (\Gamma \nabla \phi) = -S_\phi \quad (3.23)$$

If we set $-S_\phi = 0$ and $\Gamma = \varepsilon_r$, we obtain the Poisson equation for the electric potential field (Equation 3.14). Furthermore, if we set $\phi = \rho_c$, $\Gamma = \varepsilon_r$ and $-S_\phi = \frac{\rho_c}{\lambda_d^2}$ we obtain the Helmholtz equation that needs to be solved for the net charge density field (Equation 4.4). Therefore, we could use this function within Fluent to compute the two differential equations for the electric potential field and the net charge density field.

Two separate UDS Transport Equations have to be set, one for the electric potential ϕ and one for the net charge density ρ_c . The boundary conditions can be set in the fluid zone and in the solid boundaries. Now that we have the UDS Transport Equations, only a small bit of programming is needed to obtain the solutions. Fluent gives the possibility to use a so-called User-Defined Function (UDF) which has to be written in the programming language C. A UDF is used to program the following parts of the computation:

- Source term of the Helmholtz equation $\frac{\rho_c}{\lambda_d^2}$
- Body force computation \vec{f}_b from ϕ and ρ_c
- Charge density distribution function boundary condition on the wall $G(x)$
- Calculation of Electric field strength E_x and E_y

The UDF used can be found in Appendix A. The main advantages of the UDS Transport Equations are that it is possible to compute the UDSs (in this case ϕ and ρ_c) fully decoupled from the flow computations and the calculation of these variables are computationally fast.

3.2.2 Code Verification

After implementation of the model of Suzen & Huang in Fluent, it is important to verify that the model works correctly and that we compute with the correct order of accuracy. The process of determining that a code accurately represents the underlying mathematical model and its solution is called *Code Verification*. In addition, Code Verification involves error evaluation from a known (analytical) solution. The Method of Manufactured Solutions (MMS) as described by Roache [20] provides a procedure to perform Code Verification .

The idea of the MMS procedure is to manufacture an exact solution, whether it is physical or not is not relevant. A non-physical solution can be used because Code Verification is a purely mathematical exercise and therefore does not concern the physics. In order to verify the code, the following test is applied. Suppose we have an exact solution f^{exact} and a discrete solution f^Δ . Roache describes that for a p order, the error in the solution asymptotically will be by definition proportional to Δx^p , see Equation 3.24 (where H.O.T. are Higher Order Terms). In the computation of ϕ and ρ_c , a second order method is used. Therefore, the error should be proportional to Δx^2 . This should yield by definition a slope of 2 in a log-log graph of the error plotted against the cell width (Δx), if the grid is sufficiently refined. This test will be applied to verify the code.

$$\text{Error} = f^\Delta - f^{exact} = C\Delta^p + \text{H.O.T.} \quad (3.24)$$

The procedure is as follows:

1. Choice of a benchmark non-trivial and continuous solution
2. Determination of the source term that produces the benchmark solution
3. Set-up boundary conditions that correspond to the benchmark solution
4. Solve the problem
5. Perform discretization convergence tests to determine the order of convergence

Roache claims that if the discretization convergence test indeed converges with a slope of p , the code verifies:

1. the order of the discretization
2. the encoding of the discretization
3. the matrix solution procedure
4. any coordinate transformation used

Note that the fourth point is not in the scope of this work, due to the fact that only rectangular domains are used. In the model of Suzen & Huang there are two different equations which are solved (Equations 3.14 and 4.4). Therefore, two MMS procedures have to be conducted, one for every equation.

Electric potential ϕ MMS procedure

The PDE for the electric potential ϕ can be written as (assuming $\varepsilon_r = 1$ which does not change the form of the equations):

$$\nabla^2 \phi = 0 \quad (3.25)$$

The first step is to choose a benchmark non-trivial continuous solution. Roache suggests to use a Sine shape solution. The chosen solution is:

$$\phi(x, y) = \sin(x + by) \quad (3.26)$$

with b being an arbitrary constant. A plot of this chosen solution can be found in Figure 3.5. The next step is to calculate the source term $S(x, y)$ that produces this analytical solution. To do this, Equation 3.25 is written in an operator form and set equal to the source term:

$$L(\phi) = \nabla^2 \phi(x, y) = S(x, y) \quad (3.27)$$

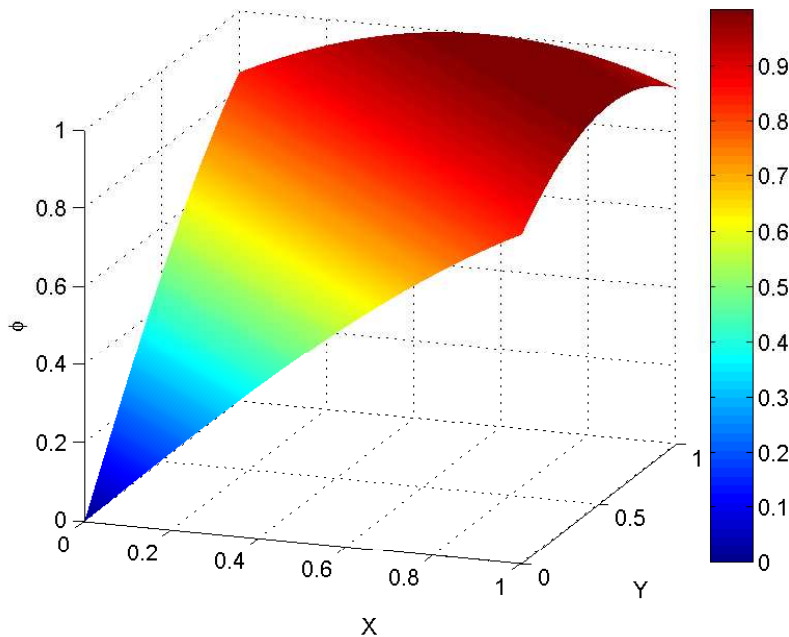


Figure 3.5: Plot of $\phi(x, y)$ in the chosen domain

This results in the following source term:

$$S(x, y) = \nabla^2 \phi(x, y) = -(1 + b^2) \sin(x + by) \quad (3.28)$$

For the sake of simplicity, a rectangular domain used: $0 \leq x \leq 1$ and $0 \leq y \leq 1$. This domain results in the boundary conditions found in Table 3.1.

In order to perform the grid convergence test, several cases are run with varying number of cells. The measured quantity will be the integral of ϕ over the domain. Because we are using an analytical solution, the integral of this analytical solution is exact.

Location	Boundary Condition
$x = 0$	$\phi(0, y) = \sin(by)$
$x = 1$	$\phi(1, y) = \sin(1 + by)$
$y = 0$	$\phi(x, 0) = \sin(x)$
$y = 1$	$\phi(x, 1) = \sin(x + b)$

Table 3.1: Boundary conditions MMS procedure

$$\int_0^1 \int_0^1 \phi(x, y) dy dx = \int_0^1 \int_0^1 \sin(x + by) dy dx = \frac{(\sin(b) + \sin(1) - \sin(1 + b))}{b} \quad (3.29)$$

b is an arbitrary constant. Therefore if we take $b = 1$ we obtain:

$$\int_0^1 \int_0^1 \sin(x + by) dy dx = 2\sin(1) - \sin(2) \approx 0.7736445 \quad (3.30)$$

The PDE for the electric potential ϕ is solved using a second order discretization. The simulations are conducted with square cells of varying width (or height).

Cell width [m]	Error w.r.t. exact solution [%]
0.1	0.1590
0.01	0.0016
0.001	2.8279E-5

Table 3.2: Errors MMS simulations

In Table 3.2 one can see the simulations conducted together with the error with respect to the analytical solution. A log-log graph of the cell width with the corresponding errors can be found in Figure 3.6. As predicted, the slope of the graph has a value of 2. Therefore the code is verified.

Charge density ρ_c MMS procedure

The procedure of the electric potential ϕ is also used for the charge density ρ_c equation. Again, taking $\varepsilon_r = 1$ which does not change the form of the equation, the equation for the charge density reduces to:

$$\nabla^2 \rho_c(x, y) = \frac{\rho_c}{\lambda_d^2} \quad (3.31)$$

$$\rho_c(x, y) = \sin(x + by) \quad (3.32)$$

with b being an arbitrary constant. A plot of this chosen solution can be found in Figure 3.5. The next step is to calculate the source term $S(x, y)$ that produces this analytical solution. To do this, Equation 3.31 is written in an operator form and set equal to the source term:

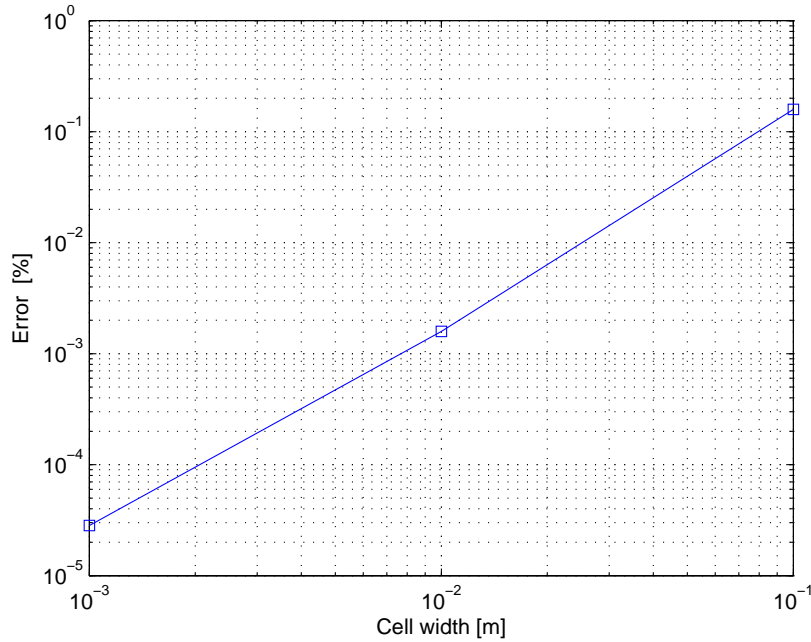


Figure 3.6: Plot of the Error vs. Cell width

$$L(\phi) = \nabla^2 \rho_c(x, y) - \frac{\rho_c(x, y)}{\lambda_d^2} = S(x, y) \quad (3.33)$$

This results in the following source term:

$$S(x, y) = \nabla^2 \rho_c(x, y) = -\left(1 + \frac{1}{\lambda_D^2} + b^2\right) \sin(x + by) \quad (3.34)$$

If we compare this source term with the source term obtained for the electric potential ϕ MMS procedure (Equation 3.28), we see that they are almost similar. The source term for the charge density has an extra constant term ($\frac{1}{\lambda_d^2}$) in the amplitude of the source term. Furthermore, the boundary conditions are similar. Therefore, we can conclude that this is a similar problem as worked out for the electric potential only with a larger amplitude. Because the code verification succeeded for the electric potential ϕ , the code for the charge density ρ_c is also verified.

3.2.3 Configuration and Numerical Set-up

Suzen & Huang do not give information about the used computational grid and domain. This leaves us in some difficulty regarding obtaining an exactly corresponding solution to that obtained by Suzen & Huang. The dimensions of the configuration used by Suzen & Huang can be found in Figure 3.7.

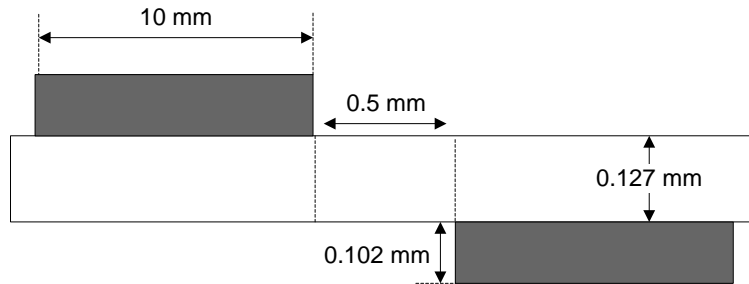
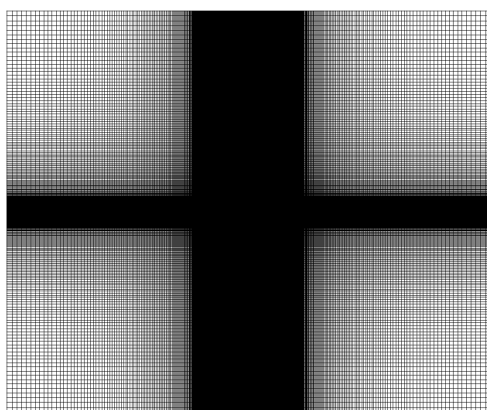


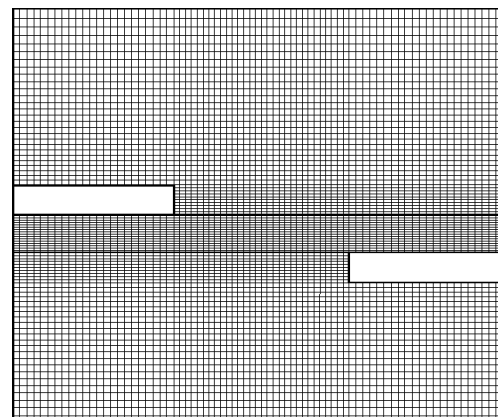
Figure 3.7: Configuration dimensions used by Suzen & Huang

Due to the rectangular computational domain and bodies (electrodes and dielectric), use is made of a rectangular two-dimensional grid. This rectangular grid is built-up in a structured manner in order to minimize the number of cells. Several cases are run with different grid resolution and domain size (see Section 3.3.4). Figure 3.8(a) shows the reference grid. This grid is a reference grid for the domain and grid independence studies. The cell density increases near the electrodes, in order to capture the important physics at these locations. Therefore, the grid refinement is applied at these regions. For a zoomed view of the grid near the electrodes, see Figure 3.8(b).

The outer boundaries are set with the pressure-outlet boundary condition option in Fluent. When using the pressure-outlet boundary condition, Fluent uses the pressure set as the static pressure of the fluid at the outer boundary and extrapolates all other conditions from the interior of the domain. A second order discretization is used for pressure and momentum. The SIMPLE algorithm is used for the pressure-velocity coupling.



(a) Reference numerical grid



(b) Reference numerical grid zoomed view

Figure 3.8: Grid used for validation of model of Suzen & Huang

3.3 Validation Electrostatic Model

3.3.1 Notes regarding Suzen & Huang simulations

Before comparing the obtained body force field f_b , electric potential field ϕ , charge density field ρ_c and streamlines with the results obtained by Suzen & Huang, it is important to note the following. The works of Suzen & Huang leave us with some uncertainties and inaccuracies. In the works of Suzen & Huang, no description is given of the numerical set-up. The size of the domain, the number of cells and cell size are all unknown variables. Furthermore, Suzen & Huang obtain a jet with a maximum velocity of approximately 1 m/s. The phrase 'approximately' is cited from the works of Suzen & Huang. This phrase leaves us with an unknown error margin in the maximum velocity. Therefore, it is expected that the simulation will qualitatively yield the same results as obtained by Suzen & Huang. However, because there are a lot of unknown parameters (as described above), there could be some quantitative differences between the simulations. Therefore, the flow field simulation is compared to the experimental results obtained by Jacob et al [12].

3.3.2 Electric potential, charge density and body force

Use is made of non-dimensional variables. Therefore, as said earlier, it is possible to solve for an unsteady actuation case both UDS equations prior to the computation of the flow field. In Figure 3.9 one can see a comparison of the electric potential contours obtained by Suzen & Huang and the current simulation. The results of the current simulation agrees well with the potential field found by Suzen & Huang. The largest gradient in electric potential can be found in the area between the electrodes. Therefore, by definition this is the region where the electric field is the strongest. There is a small difference in the contour lines at the interface between dielectric and air. This is caused by the method used to set the diffusion coefficient Γ (or relative permittivity ε_r) in Fluent. Suzen & Huang set a mean relative permittivity on the edge between the electrodes, see Figure 3.4(a). In Fluent it is not possible to set a diffusion coefficient on an edge. It is only possible to set this in a face region. Therefore the choice is made to use a discontinuous relative permittivity. This results in the kink in the contour lines at the interface. In the body force force plots, we will see that the influence of these kinks is negligible. There is a larger difference however in the streamlines. In the results of Suzen & Huang, the streamlines arrive more vertically from the upper region of the field of view. Furthermore, the streamlines end up concentrated in the region above the right electrode. It should be noted that the field of view is very small (2.5mm x 0.6mm) and the complete flow field does agree well with the results of Suzen & Huang (see Section 3.3.3).

In Figure 3.10 one can see a comparison of the contours of the charge density ρ_c . The results match the contours as obtained by Suzen & Huang well. The only significant difference, is in the region between both electrodes. The results of Suzen & Huang (Figure 3.10(a)) show a smaller gradient of the charge density as one moves from the left to the right electrode. The current simulation (Figure 3.10(b)), this gradient is larger and more concentrated near the region above the left edge of the encapsulated electrode.

In Figure 3.11 one can see a comparison of the contours of the body force f_b . Again the results correspond well with the contour plot of Suzen & Huang. Suzen & Huang obtain a maximum normalized body force of $f_{bmax} = 1250$, in the current simulation $f_{bmax} = 1444$ and acts in a small area compared to the total body force field. The error is approximately 15%. The rest of the body force field magnitudes correspond well with the values obtained by Suzen & Huang. A parameter which would tell use more about the overall error is the integral of the body force over the domain. Unfortunately, Suzen & Huang do not compute this value in his works.

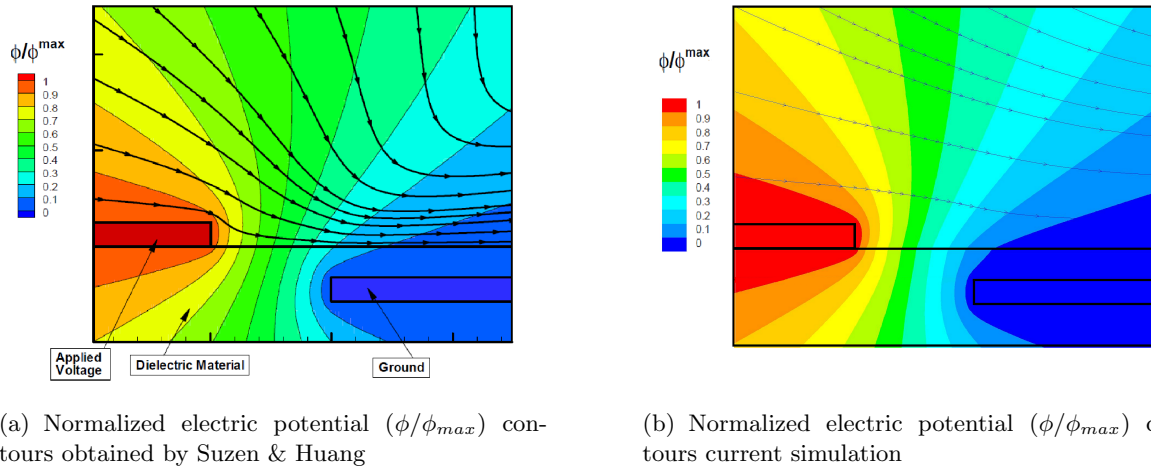


Figure 3.9: Comparison electric potential field

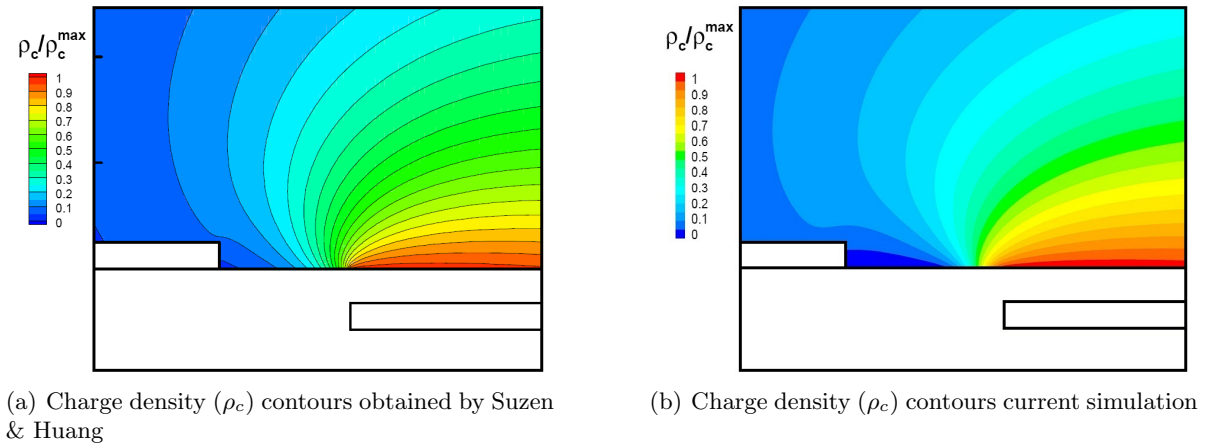


Figure 3.10: Comparison charge density field

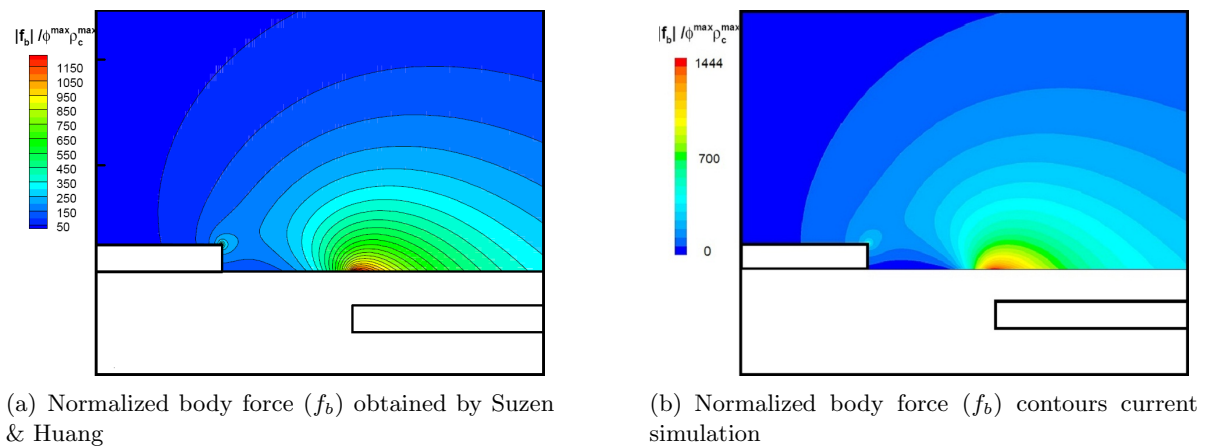


Figure 3.11: Comparison of normalized body force field

In Figure 3.12, one can see the body force profile above the left edge of the encapsulated electrode.

One can see that the maximum body force reaches its peak at a 0.1mm from the wall. Furthermore, in Figure 3.13, one can find the obtained body force vector field. The body force is directed upwards (relatively small body force magnitude) above the exposed electrode and downwards (relatively large body force magnitude) above the encapsulated electrode.

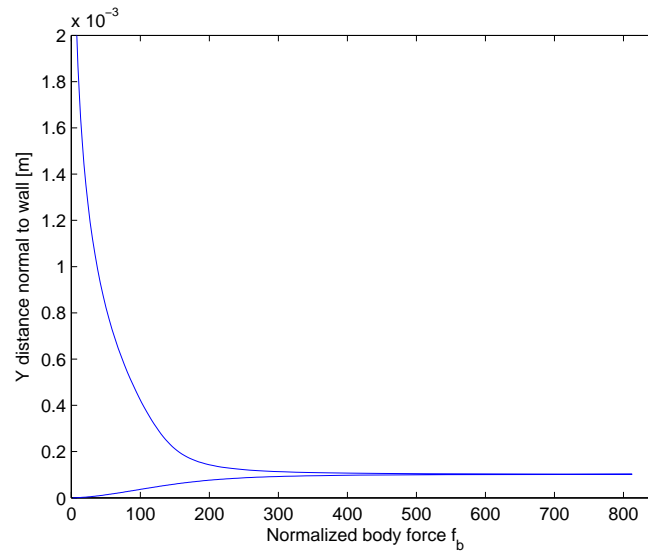


Figure 3.12: Profile of the body force f_b above left edge of encapsulated electrode

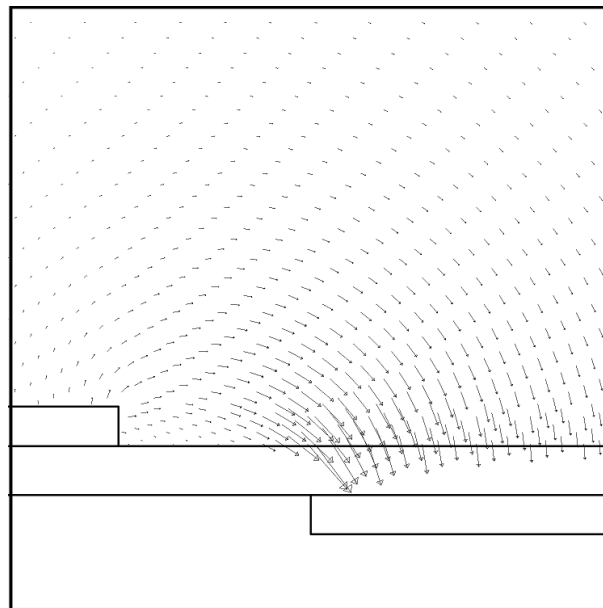


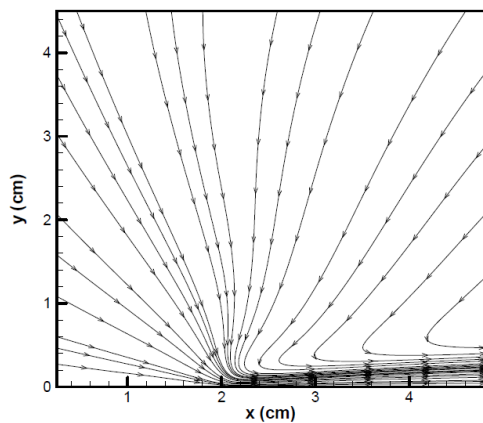
Figure 3.13: Body force vector field

3.3.3 Quiescent flow simulation

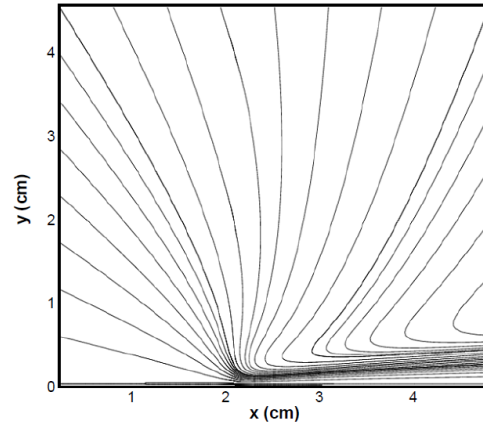
In Figure 3.14 one can find the obtained flow field compared to the flow field found by Suzen & Huang and the experimental flow field found by Jacob [12]. It is clear that overall the flow field obtained corresponds well with the flow field obtained by Suzen & Huang. However, the current

simulation shows slightly curved streamlines above right edge of the exposed electrode ($x = 2\text{cm}$), where the streamlines of Suzen & Huang are more straight when approaching the electrodes. These curved streamlines however do seem to correspond with the streamlines obtained experimentally by Jacob. The jet thickness at $x = 5\text{cm}$ in the current simulation is approximately 1mm thicker than the jet thickness obtained by Suzen & Huang. The experimental jet thickness is even thicker.

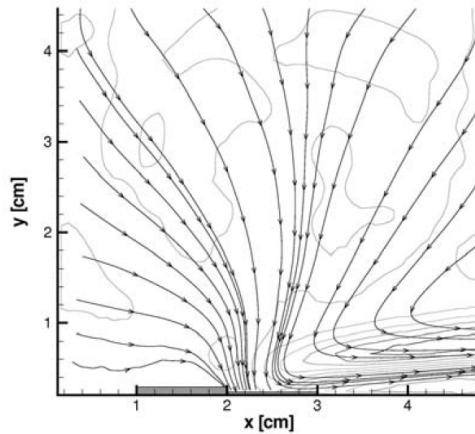
The difference in streamline pattern can be due to the unknown computational set-up used in the simulations of Suzen & Huang. Therefore it is difficult to obtain a exactly similar streamline pattern in the current simulation. Qualitatively, these results are sufficient because the most important flow area (the synthetic jet) is captured well. The plasma actuator attracts the flow from the surrounding area and pushes it as a jet from the exposed to the encapsulated electrode direction.



(a) Streamlines near electrodes obtained by Suzen & Huang



(b) Streamlines obtained current simulation



(c) Streamlines obtained experimentally [12]

Figure 3.14: Comparison of streamlines near electrodes for $0 \leq x \leq 50\text{mm}$ and $0 \leq y \leq 45\text{mm}$

3.3.4 Domain and Grid studies

The following approach is used to ensure that the obtained solution is both domain and grid independent. The reference grid is primarily solved. Two different grids are generated by building blocks around the reference grid. Therefore the maximum grid resolution is equal to the reference grid, however the domain is larger. The measured quantity is the maximum velocity in the domain and it is compared to the obtained maximum velocity from experiments [12] and numerical simulations done by Suzen & Huang. Jacob obtained a maximum velocity of 1 m/s.

When the domain-independent solution is found, the largest domain is used and grid refinement is applied to obtain a higher grid resolution in the area with the largest velocity gradients. Two grids are built with increasing number of cells. Again the measured quantity is the maximum velocity in the domain. This will yield both a domain and grid independent solution.

In Table 3.3 one can see the results of the domain independence study. The error in maximum velocity is 7.94% for the smallest domain and 7.75% for the largest domain. This shows that the error does not change significantly $\approx 2\%$ with increasing domain size. Figure 3.15(a) shows the graph of the error in maximum velocity plotted against the domain size.

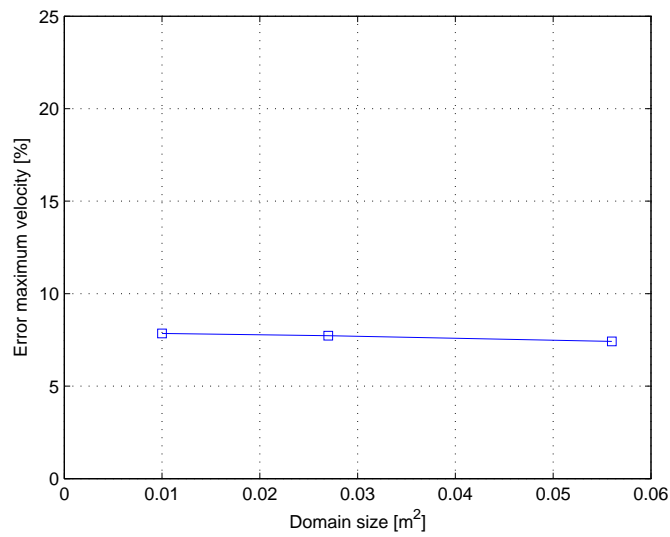
Domain size [m^2]	Number of Cells	Maximum velocity	Error maximum velocity [%]
0.01	213200	0.92153	7.85
0.027	232100	0.92276	7.72
0.056	254334	0.92582	7.42

Table 3.3: Results of the domain independence study

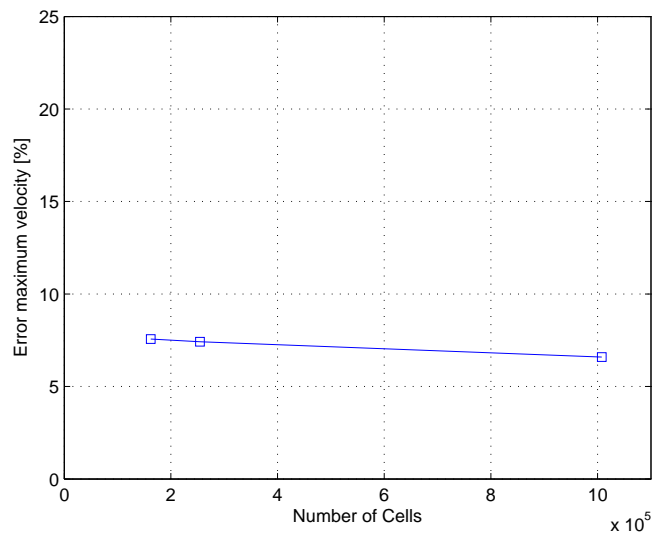
In Table 3.4 one can see the results of the grid independence study. The error in maximum velocity is 7.94% for the case with the lowest number of cells and 7.54% for the grid with the largest number of cells. This shows that the error does not change significantly ($\approx 5\%$) with increasing cell density. This error is certain with respect to the experimental data. However compared to the simulation of Suzen & Huang, this error could be significantly less. As mentioned earlier, Suzen & Huang only give an approximate value of 1m/s and therefore leaves an unknown error margin. Figure 3.15(b) shows the graph of the error in maximum velocity plotted against the number of cells.

Domain size [m^2]	Nr. of cells	Smallest cell size [m]	Max. velocity [m/s]	Error max. velocity [%]
0.056	162176	$1 \cdot 10^{-5}$	0.92436	7.56
0.056	254334	$5 \cdot 10^{-6}$	0.92582	7.42
0.056	1007748	$1 \cdot 10^{-6}$	0.93407	6.59

Table 3.4: Results grid of the independence study



(a) Plot of the Error in maximum velocity vs. the Domain size



(b) Plot of the Error in maximum velocity vs. the Number of cells

Figure 3.15: Results domain and grid independence

Generalization of the Suzen & Huang model

4.1 Introduction

The previous chapter resulted in validation of the model of Suzen & Huang for one specific case: One specific electrode configuration and one applied voltage (5kV). The goal of having a plasma actuator model is the possibility to mimic the plasma actuator in different configurations and input voltages. This variety of parameters then allows to efficiently study aerodynamic phenomena caused by the actuator with CFD, rather than building every test case in real life. This chapter will research methods to generalize the model of Suzen & Huang in order to apply it with various input voltages and configurations. The application of different voltages is coupled to the important relation between the induced maximum velocity and the applied voltage discussed in Section 2.2.5. We have found that the configuration used by Suzen & Huang induces a jet velocity of approximately 1m/s. For effective aerodynamic flow control purposes, a larger jet velocity is needed. The most straightforward way to obtain a larger jet velocity is to increase the input voltage. The model of Suzen & Huang uses normalized body forces and therefore multiplication by a larger input voltage will yield a larger body force and therefore a larger induced jet velocity. From literature it is known that the generated thrust should increase as $V^{7/2}$ [5]. This proportionality also holds for the generated total body force. One can say that $f_b = Thrust = U_{max} \propto V^{7/2}$

Now let us analyze the capability of the model of Suzen & Huang to obtain this relation of $f_b \propto V^{7/2}$. The model of Suzen & Huang calculates a normalized body force obtained from the electric potential and charge density fields. This normalized body force is multiplied by the input voltage and the maximum charge density ($\rho_{max} V_{app}$). Now if we assume that ρ_{max} increases proportionally to the input voltage V_{app} , we find that the generated total body force increases as $f_b \propto V^2$. This shows that the model of Suzen & Huang under predicts the generated body force when using a different input voltage. This discrepancy can be explained by two incapacibilities of the model of Suzen & Huang:

1. The model is unable to simulate the growth of the volume of the plasma as a function of input voltage.

2. The model does not take into account the charge build-up on the surface above the encapsulated electrode as a function of input voltage.

In order to generalize the model of Suzen & Huang, the above two incapacibilities of the model have to be overcome. The first point, growth of the plasma volume as a function of input voltage, can be realized by modification of the charge density distribution function on the surface above the encapsulated electrode. Suzen & Huang use a Gaussian distribution function on the surface. A method of incorporating growth in plasma volume as a function of input voltage is the addition of one degree of freedom to the distribution function of the charge density. This degree of freedom is the input voltage. An additional parameter which could be changed is the Debye length. A larger Debye length will increase the volume of the plasma and vice versa. It is known from literature that physically the Debye length for the plasmas under consideration is more or less a fixed parameter, however calibration within the order of magnitude of $\lambda_d = 0.00017m$ is allowed.

The second point, the charge build-up on the surface above the encapsulated electrode, is given in the model of Suzen & Huang by the parameter ρ_c^{\max} . Suzen & Huang used a fixed value for this parameter. This parameter could be made a function of the input voltage in order to account for the charge build-up as a function of input voltage. Both points are a modification of the charge density field and thus the electric potential field remains unchanged.

4.2 Benchmark experimental data

In order to analyze the applicability of the model of Suzen & Huang in different configurations using the above two points, experimental data is needed as a benchmark to give us a modification of the model based on physics. Currently in literature there is one source with experimentally measured body force fields available: Kotsonis et al [15]. The works of Kotsonis offer body force fields for different input voltages obtained from PIV measurements together with a full Navier-Stokes term decomposition. The plasma actuator configuration used by Kotsonis consists of electrodes with a width of 10 mm and $60\mu\text{m}$ thickness. A zero horizontal gap is used between the electrodes. Furthermore, the electrodes are separated by two dielectric layers of polyimide Kapton tape with a total thickness (including adhesive layer) of $110\mu\text{m}$. The input peak-to-peak voltage on the electrodes was varied from $8kV_{pp}$ to $16kV_{pp}$ with a step size of $2kV_{pp}$. The body force field is measured for every input peak-to-peak voltage. The configuration used by Kotsonis can be found in Figure 4.1.

Because the previously mentioned two generalization points do not change the potential field, we can use the body force measurements to obtain the charge density fields. To obtain the corresponding charge density fields, use is made of Equation 3.17. This equation shows that the charge density field can be obtained by dividing the body force field \vec{f}_b by the electric field $\vec{E} = -\nabla\Phi$. The electric field is taken at the peak of the voltage cycle. The obtained charge density field for different voltages will be a benchmark for the generalization of the model of Suzen & Huang. For the sake of simplicity we will focus on the horizontal component of the body force. If we are able to generalize the model to fit this horizontal component the vertical component will also be physically correct. This is due to the net charge density ρ_c being a scalar, correct modeling of this parameter together with equal electric potential field should yield the correct horizontal and vertical body force components.

Kotsonis' configuration is modeled with CFD using the model of Suzen & Huang to obtain the electric potential field for this geometry. A grid is constructed with a smallest cell size of $1 \cdot 10^{-6}\text{m}$ located at the interface between both electrodes. The grid convergence study conducted in Chapter

4.3 Extraction of charge density field from experimentally obtained body force field

3 showed that this cell size is small enough to capture the plasma physics of interest. A domain size of $0.1 \times 0.1 \text{ m}$ is used. Because the simulations do not contain a flow computation, this domain size is large enough to damp out the influence of the outer boundaries on the areas of interest near the electrodes.

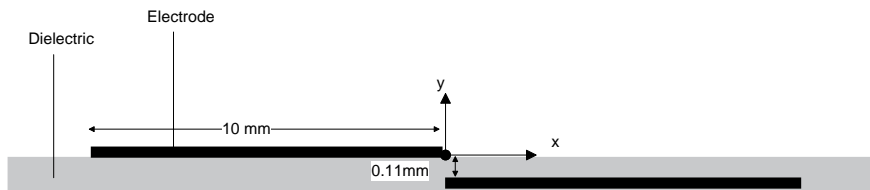


Figure 4.1: Actuator configuration used by Kotsonis et al [15]

4.3 Extraction of charge density field from experimentally obtained body force field

In Figure 4.2, one can see the electric potential field ϕ and the corresponding horizontal component of the electric field E_x obtained using the model of Suzen & Huang [25] applied on the configuration used by Kotsonis. A normalized electric potential field is used, therefore a normalized electric field strength is calculated. This allows the recalculation the electric field strength for every applied voltage simply by multiplication of the normalized electric field by the applied voltage. The horizontal component of the electric field is concentrated in the area between both electrodes where the largest gradient in electric potential is located.

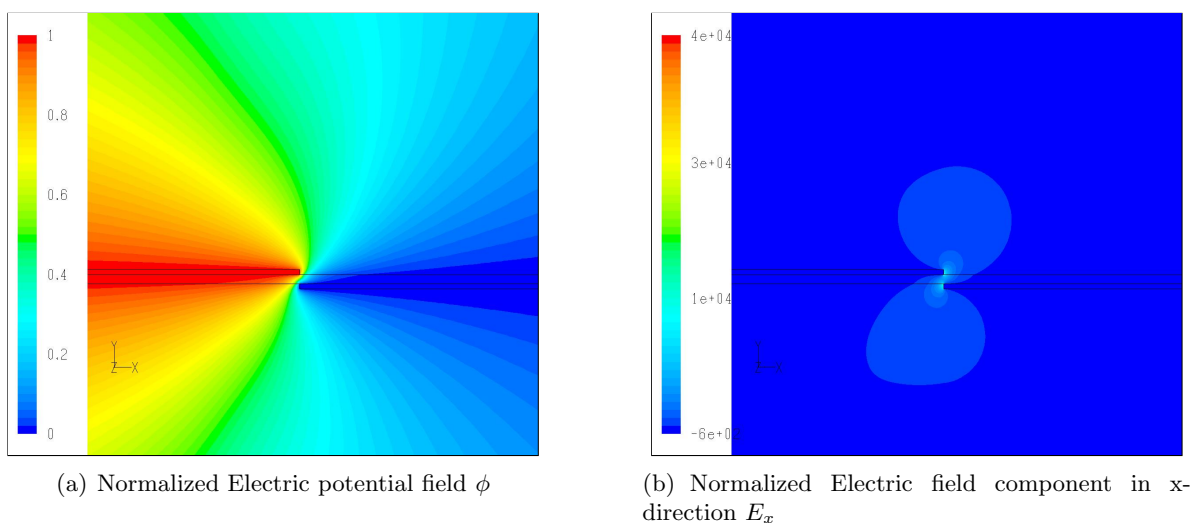


Figure 4.2: Comparison of normalized body force field

Kotsonis measured in a domain of $-1\text{mm} \leq x \leq 7\text{mm}$ and $0 \leq y \leq 2\text{mm}$. This measurement domain resulted in a matrix of (322,74) (X,Y) data points. The grid used to obtain the electric potential field and the corresponding horizontal electric field component is much finer. Therefore, the data has to be interpolated from the CFD grid to a 322x74 array. This is done with a so-called *griddata* function in Matlab. Griddata is a function that uses a so-called biharmonic spline interpolation method, documented in the works of Sandwell [22]. Spline interpolation is an interpolation method that uses an interpolant that is a special type of piecewise polynomial (spline). The interpolated horizontal component electric field on a 322x74 matrix can be seen in Figure 4.3.

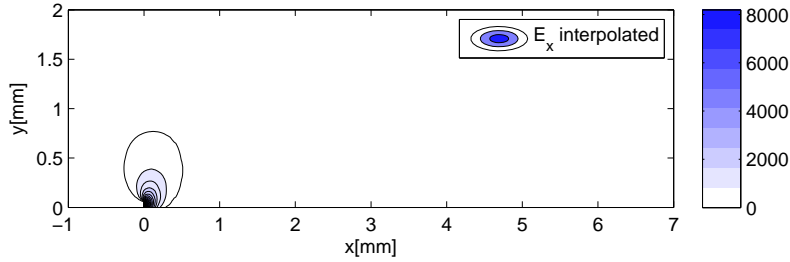


Figure 4.3: Interpolated horizontal electric field component E_x

In Figure 4.4, one can see the horizontal component of the body force field obtained by Kotsonis. The plasma volume, represented by the body force field, clearly increases when the input voltage is increased (note that $V_{pp} = 2V_{in}$). The width of the plasma volume increases approximately proportionally to the increasing input voltage. In addition, height of the plasma volume appears to increase with increasing input voltage. In Table 4.1, one can see the obtained integrated horizontal body force component for different input voltages. The obtained integrated body forces agree with the proportionality found in literature ($f_x \propto V^{7/2}$), see Figure 4.5.

Peak-to-peak voltage (V_{pp})	(f_x) [N]
8kV	$6.1 \cdot 10^{-4}$
10kV	0.0013
12kV	0.0032
14kV	0.0051
16kV	0.0093

Table 4.1: Integrated horizontal body force f_x obtained by Kotsonis et al

Now that we have the body force field and the electric field for this configuration, it is possible to extract the charge density field from the body force measurements conducted by Kotsonis. A division of the horizontal body force field by the horizontal component of the electric field yields the charge density field, see Figure 4.6. Similar to the horizontal component of the body force field, the charge density field increases with increasing input voltage both in width as well as in height. This is expected because the electric potential field is unchanged and therefore this change has to be similar to that observed in the body force fields.

The model of Suzen & Huang imposes a charge density distribution function on the surface above the encapsulated electrode. Therefore, it is useful to plot the charge density function on this surface, see Figure 4.7. It is clear that the charge density distribution function increases in height and width with increasing input voltages. The change in the charge density distribution function is a parameter which we would like to measure. First the maximum value of the charge density distribution is analyzed for different input voltages (see Figure 4.8). There seems to be a linear relationship

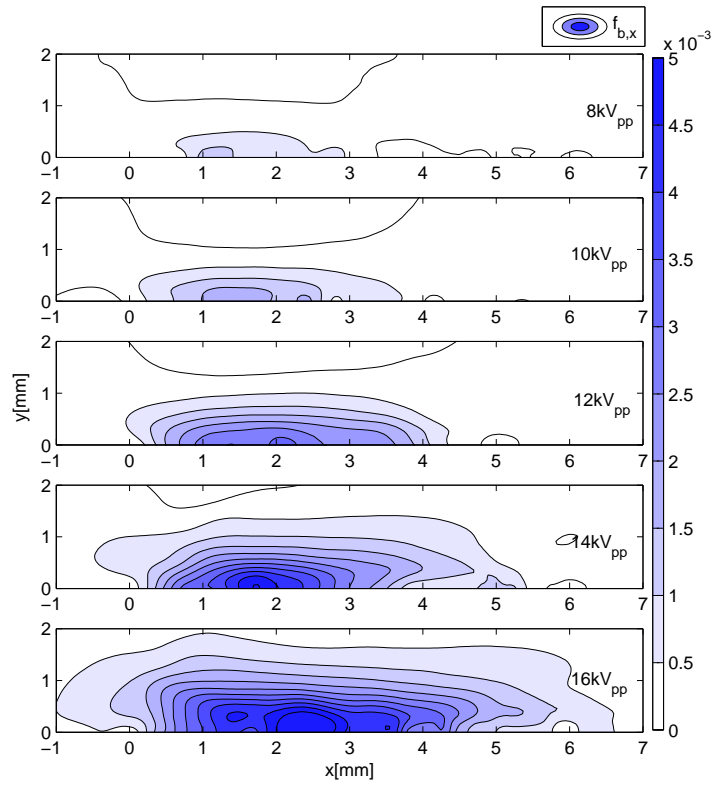


Figure 4.4: Horizontal body force component $f_{b,x}$

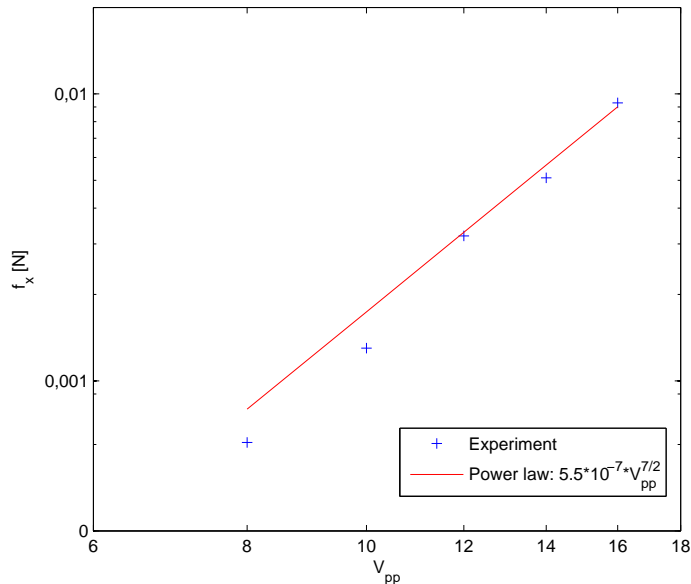


Figure 4.5: Integrated horizontal body force f_x for various voltages and curve fit

between $\rho_{c,max}$ and the input voltage. However the graphs of the charge density distribution on the wall do not have a clear maximum value, especially for larger input voltages (14 and 16 kV_{pp}).

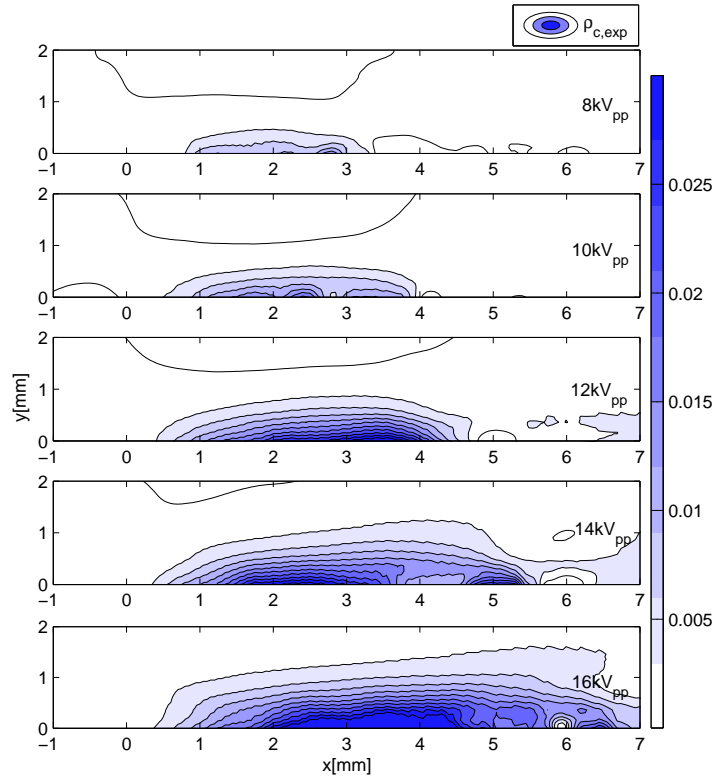


Figure 4.6: Extracted charge density field ρ_c

Therefore, the data is integrated (the area below the graph is calculated). This parameter is less noise sensitive than the maximum value. Figure 4.9 shows that the integral increases linearly with increasing input voltage. The height of the plasma is measured and plotted in Figure 4.10. The height is determined as the location where the body force is 10% of its maximum value. The plot shows us that also the height of the plasma increases linearly with increasing input voltage. This linear changing height of the plasma could give us a starting point in modeling a relation of the Debye length λ_d as a function of the input voltage. Now that we have obtained the net charge density field and some other relations, we can start working with hypotheses for model generalization.

4.3 Extraction of charge density field from experimentally obtained body force field

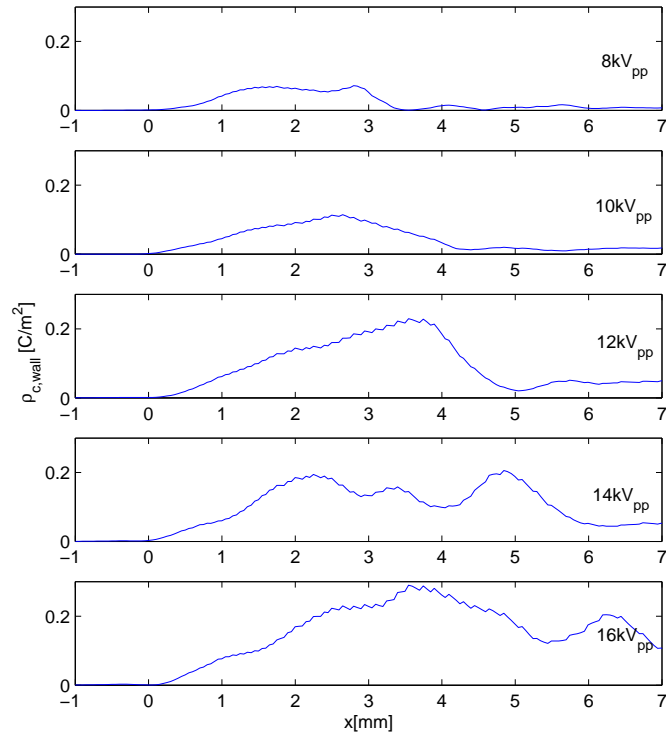


Figure 4.7: Extracted charge density profile on the wall $\rho_{c,w}$

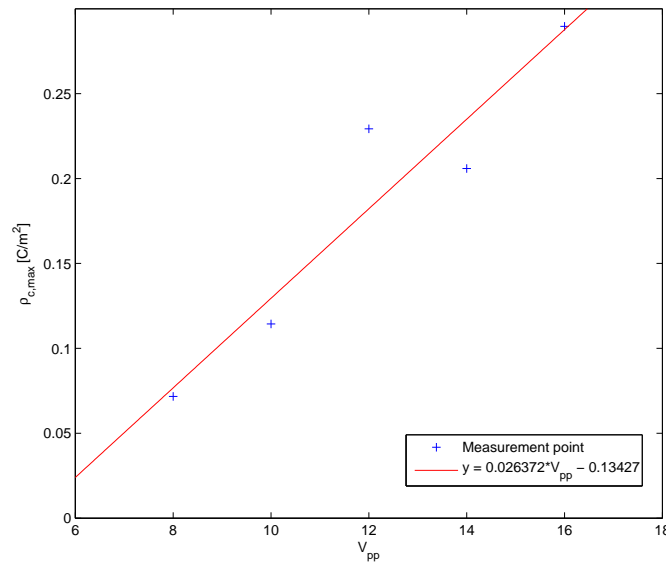


Figure 4.8: Maximum charge density $\rho_{c,max}$ against peak-to-peak voltage V_{pp}

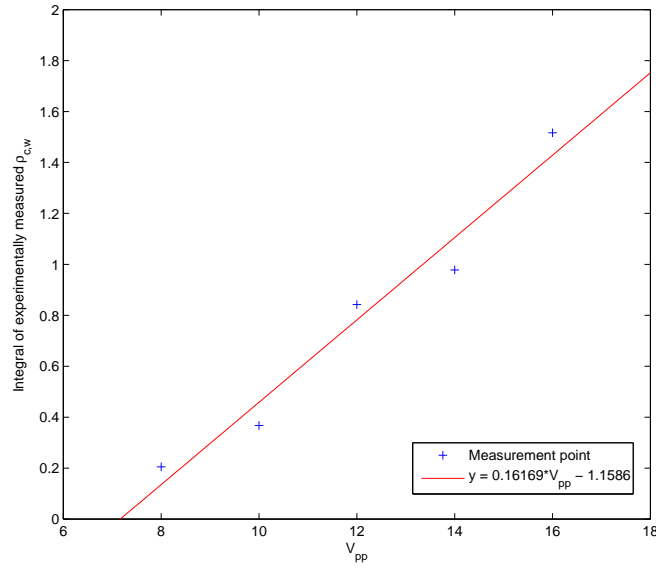


Figure 4.9: Integral of experimentally measured $\rho_{c,w}$ and curve fit

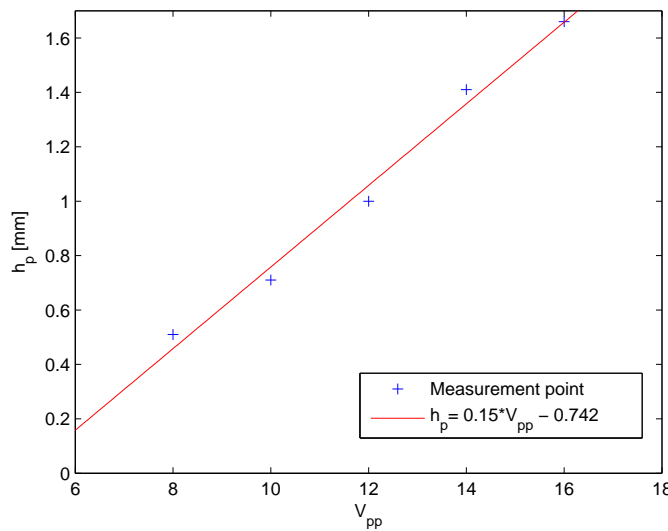


Figure 4.10: Height of the plasma h_p as a function of input voltage

4.4 Hypothesis 1: Gaussian distribution with linear changing σ and μ , Debye length constant

From Figure 4.7, one can see that the charge density profile on the wall indeed resembles a Gaussian-like distribution as suggested by Suzen & Huang. Let us use this Gaussian distribution and modify the Gaussian parameters σ and μ by making them both a function of the input voltage. It is known that the parameter μ is used for the location of the maximum value in a Gaussian distribution. The parameter σ is a measure of the width of the distribution. The Debye length is chosen in this hypothesis as a constant with a value of $\lambda_d = 0.00017\text{m}$.

A manual fit of a Gaussian distribution function with the parameters found in Table 4.2 results in the charge density on the wall as shown in Figure 4.12. The chosen Gaussian parameters are increased linearly, because we have found that both the maximum charge density on the wall as well as the integrated charge density on the wall increase linearly with increasing input voltage. Furthermore, the linear relationship for $\rho_{c,max}$ found in Figure 4.8 is used. The parameters used for Hypothesis 1 can be found in Table 4.2.

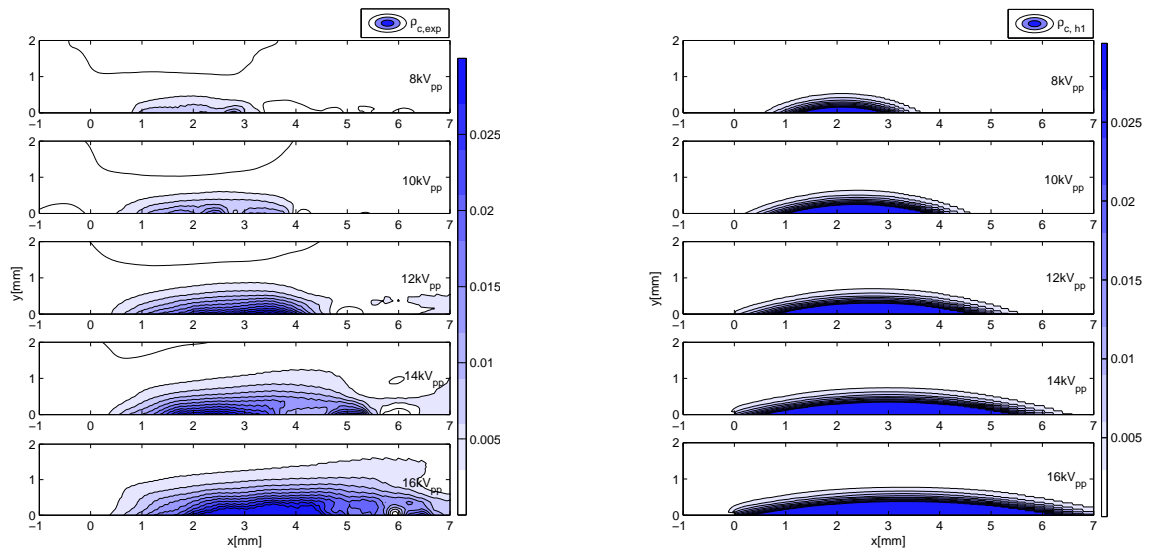
The imposed charge density on the wall resulted in a charge density field found in Figure 4.11. In this figure a comparison is shown of the experimentally obtained charge density field and the modeled charge density field. From the figure one can see that the height of the modeled charge density field is accurate with respect to the experimental height for the voltages $8kV_{pp}$ and $10kV_{pp}$. The height of modeled the charge density for the voltages $12kV_{pp}$, $14kV_{pp}$ and $16kV_{pp}$ clearly underestimates the height of the experimental charge density. The reason for this discrepancy is the fact that a constant value for Debye length is used. The width of the charge density field is more accurate. We see a small overestimation of the width for all the voltages.

V_{pp}	σ	μ	$\rho_{c,max}$
8kV	0.6	2.1	0.076706
10kV	0.8	2.4	0.12945
12kV	1	2.7	0.182194
14kV	1.2	3.0	0.234938
16kV	1.4	3.3	0.287682

Table 4.2: Gaussian parameters used for a manual curve fit

Furthermore, the modeled field overestimates the charge density in the domain $0 \leq x \leq 1\text{mm}$. This domain also contains the largest concentration of E_x and therefore the body force will be concentrated in this domain. This can be seen in Figure 4.13 where the modeled horizontal component of the body force field is demonstrated. The body force is concentrated at the right edge of the exposed electrode ($x = 0\text{mm}$). The height of the body force field is underestimated with the model for the voltages $12kV_{pp}$, $14kV_{pp}$ and $16kV_{pp}$ due to the constant Debye length. The modeled body force field is more concentrated and generally overestimated near the wall.

In Figure 4.14, one can see integrated total horizontal body force obtained using Hypothesis 1 together with the data of the experiments. Although the height of the growth in height of the body force field is not modeled, the implementation of a linear changing Gaussian distribution does result in a correct proportionality of the body force with respect to the voltage. Hypothesis 1 results in $f_x \propto V^{7/2}$. Still, the magnitude of the body force is overestimated. However this could be corrected by calibration of $\rho_{c,max}$.



(a) Charge density field extracted from experimental measurements

(b) Modeled charge density field using Hypothesis 1

Figure 4.11: Comparison of experimental and modeled charge density fields for Hypothesis 1

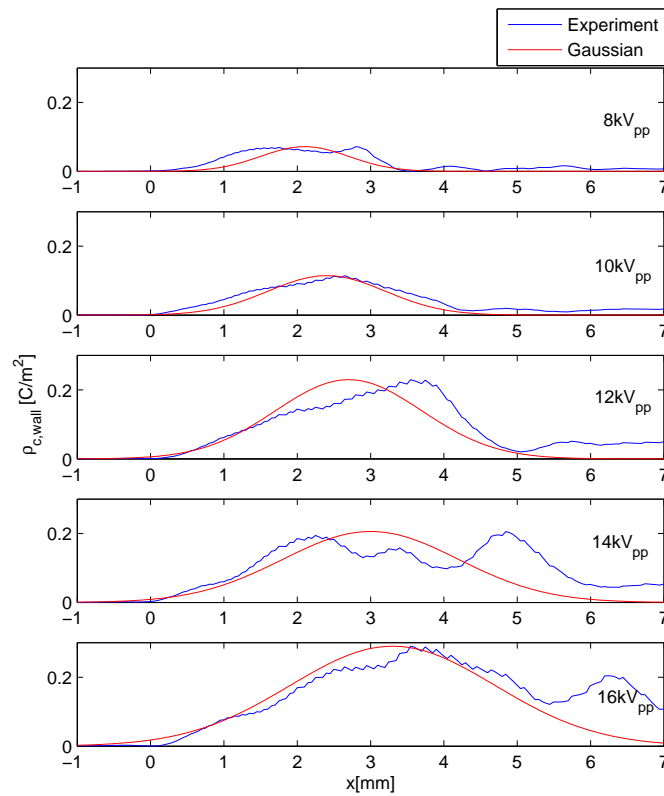
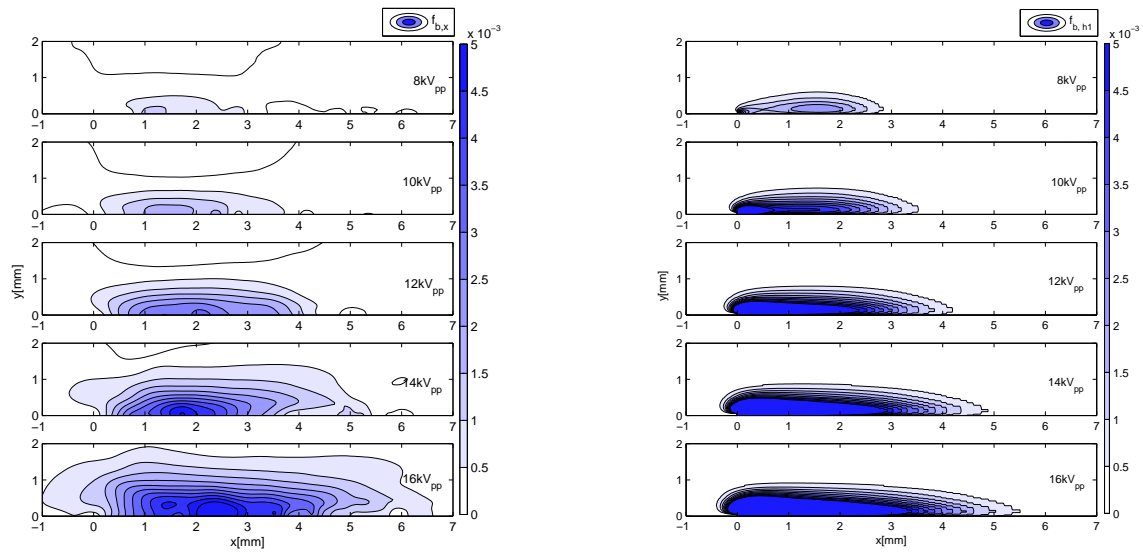


Figure 4.12: Extracted charge density profile on the wall together with a Gaussian fit



(a) Horizontal body force field extracted from experimental measurements

(b) Modeled body force field using Gaussian wall function using Hypothesis 1

Figure 4.13: Comparison of experimental and horizontal body force fields for Hypothesis 1

V_{pp}	f_x [N]
8kV	0.0021
10kV	0.0061
12kV	0.0133
14kV	0.0245
16kV	0.04

Table 4.3: Integrated horizontal body force for Hypothesis 1

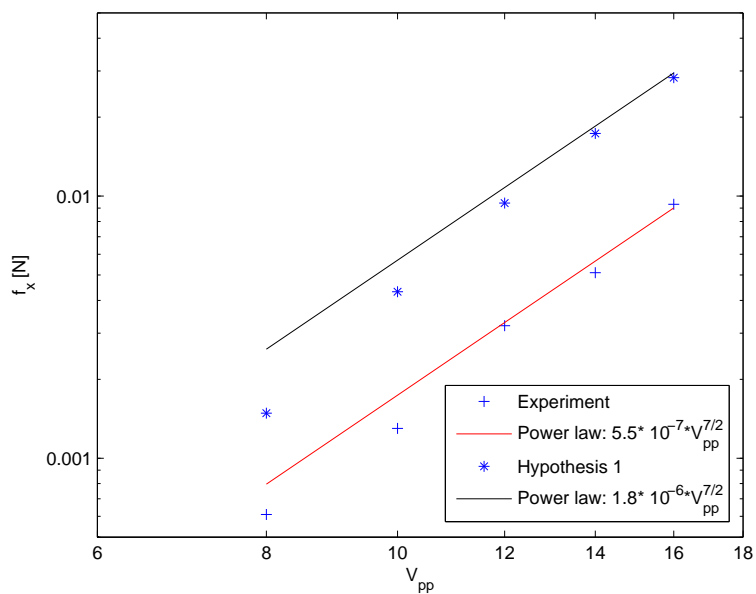
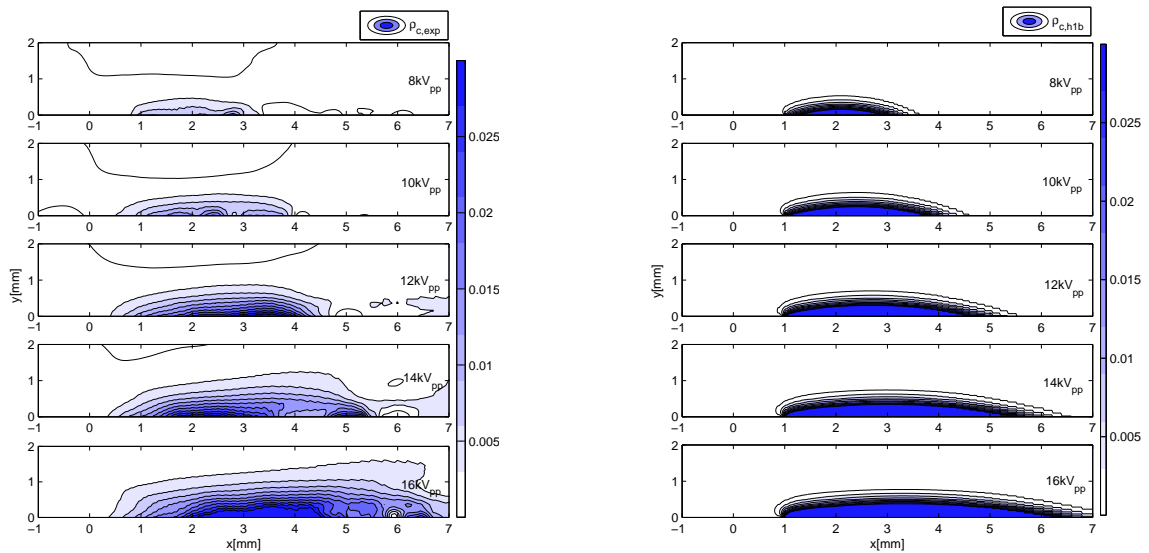


Figure 4.14: Integrated horizontal body force f_x for various voltages using Hypothesis 1

4.5 Hypothesis 1B: Gaussian distribution and zero for $0 \leq x \leq 1\text{mm}$ with linear changing σ and μ , Debye length constant

For this Hypothesis, the Gaussian distribution is taken equal to zero in the domain $0 \leq x \leq 1\text{mm}$. This is based on the fact that from Hypothesis 1 we found a significant overestimation of the charge density field and body force field in this domain. Investigation will tell us if a correction in this area, result in a more accurate integrated body force value. Note that all other parameters are equal to the parameters used in Hypothesis 1.

From Figure 4.15, one can see that indeed above the domain $0 \leq x \leq 1\text{mm}$ no concentrated charge density is present. This results in a less concentrated body force above this domain, see Figure 4.16. The body force is now concentrated in the domain above $1 \leq x \leq 3\text{mm}$ depending on the applied voltage. This is physically correct if we compare with the experimental results.



(a) Charge density field extracted from experimental measurements

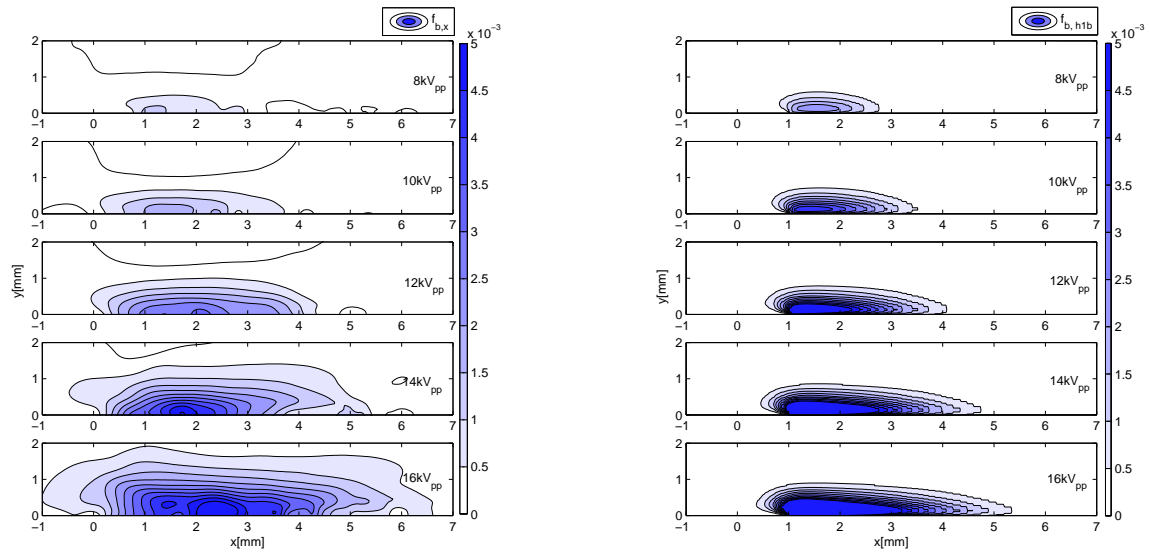
(b) Modeled charge density field using Hypothesis 1B

Figure 4.15: Comparison of experimental and modeled charge density fields for Hypothesis 1B

In Figure 4.17, one can see integrated total horizontal body force obtained using Hypothesis 1B together with the data of the experiments. Although the magnitude of the integrated body force is more accurate compared to experimental data, the proportionality is less accurate than the results obtained from Hypothesis 1. Hypothesis 1B results in $f_x \propto V^{5/2}$.

V_{pp}	f_x [N]
8kV	0.0015
10kV	0.0033
12kV	0.0058
14kV	0.0088
16kV	0.0123

Table 4.4: Integrated horizontal body force for Hypothesis 1B



(a) Horizontal body force field extracted from experimental measurements

(b) Modeled body force field using Gaussian wall function using Hypothesis 1B

Figure 4.16: Comparison of experimental and modeled horizontal body force fields for Hypothesis 1B

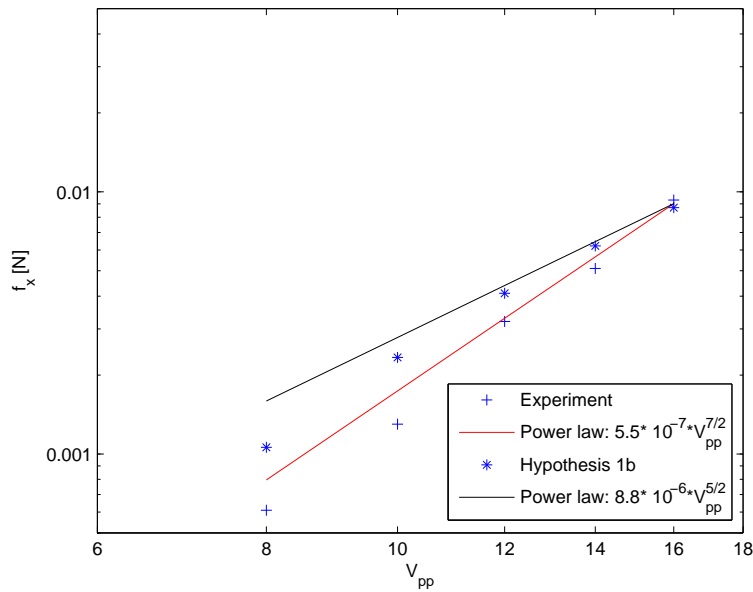


Figure 4.17: Integrated horizontal body force f_x for various voltages using Hypothesis 1B

4.6 Hypothesis 2: Gaussian distribution and zero for $0 \leq x \leq 1\text{mm}$ with linear changing σ and μ and Debye length

The underestimation of the height of the charge density field and the body force field is due to the constant value of the Debye length. Hypothesis 2 will use a linear changing Debye length value to investigate the influence of a changing Debye length on both charge density and body force field. The assumption of having a linear changing Debye length is based on the linear change in height and width of the plasma. According to Figure 4.10, the Debye length is taken to be:

$$\lambda_d[m] = K \cdot (0.15 \cdot 10^{-3}V_{pp} - 0.000742) \quad (4.1)$$

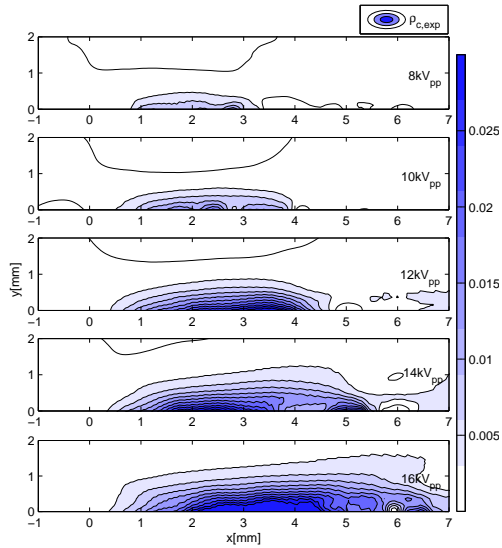
The constant K is calibrated and has a value of $K = 0.2$. This results in λ_d ranging from approximately $0.0001m - 0.0004m$. These are in the order of magnitude of the values found in literature [21].

In Figure 4.18, one can see the charge density field obtained using the assumptions of Hypothesis 2. There where Hypothesis 1 resulted in an underestimation of the charge density volume, Hypothesis 2 clearly captures the growth of the charge density volume more accurately. Furthermore, the model of Suzen & Huang causes the charge density field to increase rapidly, where the experiment shows a more gradual decay of the charge density field when moving away from the surface. This is caused by the source term in the Helmholtz equation (Equation 4.4) and therefore could not be changed without modification of the model.

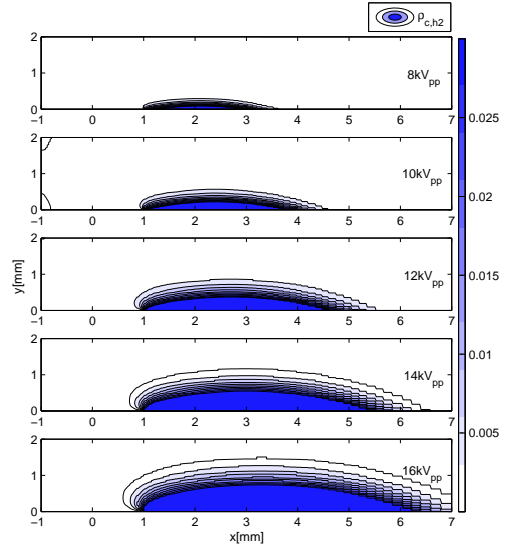
V_{pp}	σ	μ	λ_d [m]
8kV	0.6	2.1	0.0000916
10kV	0.8	2.4	0.0001516
12kV	1	2.7	0.0002116
14kV	1.2	3.0	0.0002716
16kV	1.4	3.3	0.0003316

Table 4.5: Parameters used in Hypothesis 2

In Figure 4.19, one can see the body force field obtained using Hypothesis 2. As expected due to the more accurately modeled growth of the charge density volume, the body force volume now grows with increasing input voltage. This is physically more accurate than the results of Hypothesis 1. In Figure 4.28, one can see integrated total horizontal body force obtained using Hypothesis 2 together with the data of the experiments. It is clear that the assumptions made in Hypothesis 2 do not result in an integrated body force that resembles the experimental data. The proportionality is $f_x \propto V^5$, which is a significant overestimation of the body force change with respect to input voltage.

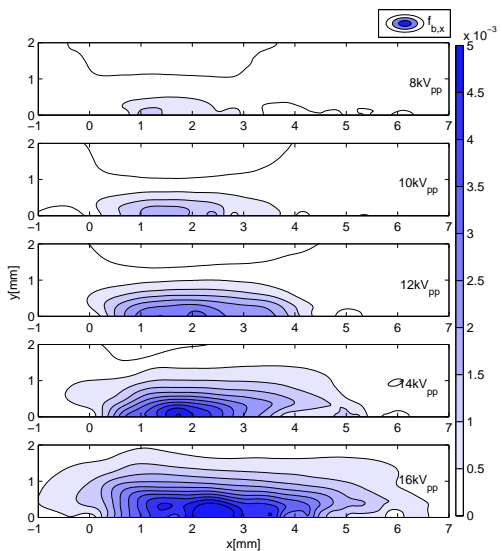


(a) Charge density field extracted from experimental measurements

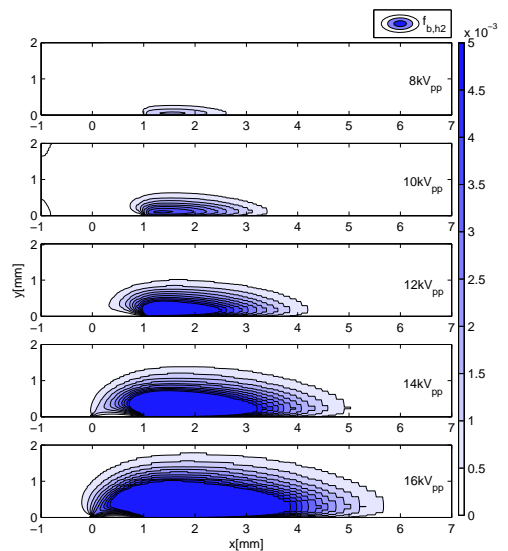


(b) Modeled charge density field using Hypothesis 2

Figure 4.18: Comparison of experimental and modeled charge density fields for Hypothesis 2



(a) Horizontal body force field extracted from experimental measurements



(b) Modeled body force field using Hypothesis 2

Figure 4.19: Comparison of experimental and modeled horizontal body force fields for Hypothesis 2

V_{pp}	f_x [N]
8kV	$5.2 \cdot 10^{-4}$
10kV	0.0027
12kV	0.0085
14kV	0.0202
16kV	0.0404

Table 4.6: Integrated horizontal body force for Hypothesis 2

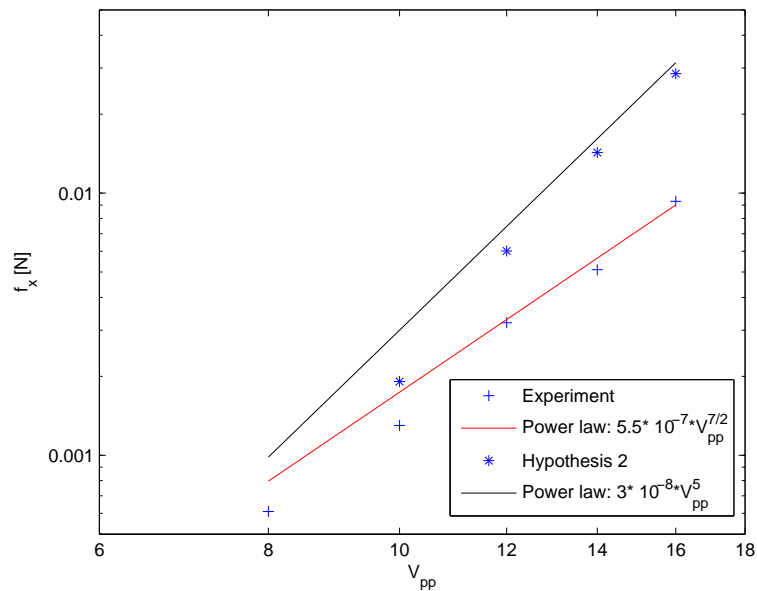


Figure 4.20: Integrated horizontal body force f_x for various voltages using Hypothesis 2

4.7 Hypothesis 3: Gaussian curve fit distribution with constant Debye length

The previous hypotheses gave us a hint that although the correct boundary conditions are applied on the wall above the encapsulated electrode, the way the model is built (especially the source term in the Helmholtz equation) the model is not able to model the charge density and body force fields accurately. This hypothesis could simply be tested by applying an accurate curve fit of the charge density distribution on the wall and see if the model is able to obtain the correct charge density and body force fields. In this hypothesis we will use a constant value for the Debye length of $\lambda_d = 0.00017\text{m}$.

For the curve fit of the charge density distribution on the wall, we will use a general Gaussian equation with the following shape:

$$f(x) = A_1 \cdot e^{-\left(\frac{x-B_1}{C_1}\right)^2} + A_2 \cdot e^{-\left(\frac{x-B_2}{C_2}\right)^2} + \dots + A_6 \cdot e^{-\left(\frac{x-B_6}{C_6}\right)^2} \quad (4.2)$$

The coefficients used for the curve fits for the different applied voltages can be found in Appendix B.

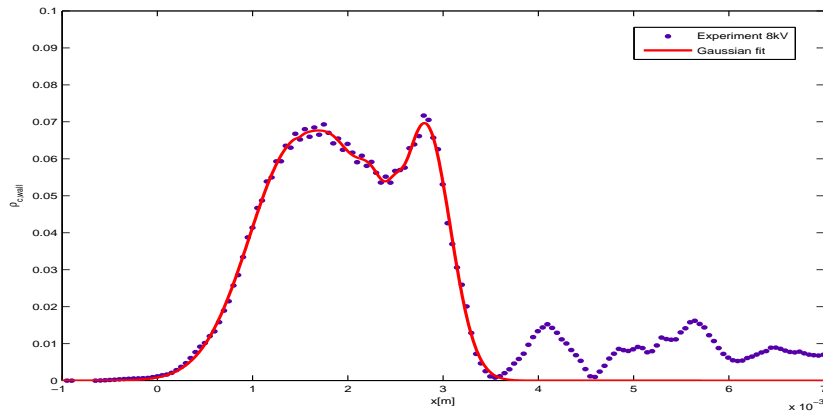


Figure 4.21: Extracted charge density profile on the wall together with a Gaussian fit for $V_{pp} = 8kV$

In Figure 4.26, one can see the charge density fields obtained using Hypothesis 3. From the figure one can see that the height of the modeled charge density field is accurate with respect to the experimental height for the voltages $8kV_{pp}$ and $10kV_{pp}$. The height of modeled the charge density for the voltages $12kV_{pp}$, $14kV_{pp}$ and $16kV_{pp}$ clearly underestimates the height of the experimental charge density. From the previous hypotheses we know that it is possible to model the changing height of the plasma by making the Debye length a function of the applied voltage. In Figure 4.27 one can see the obtained body force fields. In Figure one can see the integrated horizontal body force as a function of applied voltage. The used boundary condition result in an incorrect proportionality of approximately $f_x \propto V^{5/2}$.

Now let us focus on the charge density field for the voltages $8kV_{pp}$ and $10kV_{pp}$. We can see that the modeled charge density field height is accurate with respect to the experimental charge density field. Furthermore, we know that the imposed boundary condition is accurate. However the decay of experimental charge density field seems to be more gradual. The modeled charge density field shows a much more sudden decay. This sudden decay is modeled by the right hand side of the

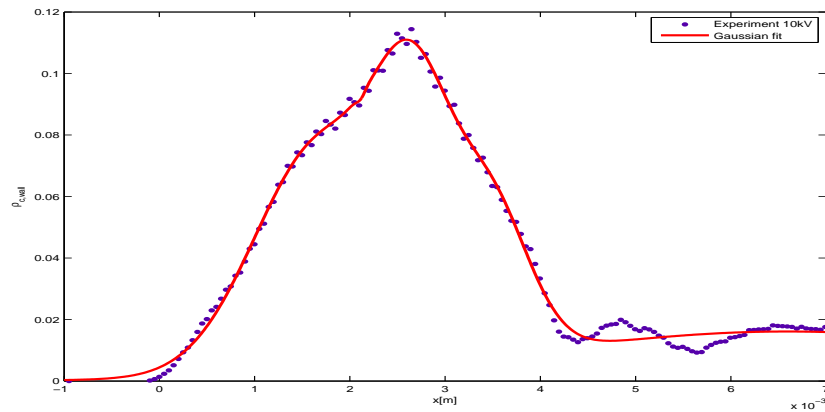


Figure 4.22: Extracted charge density profile on the wall together with a Gaussian fit for $V_{pp} = 10kV$

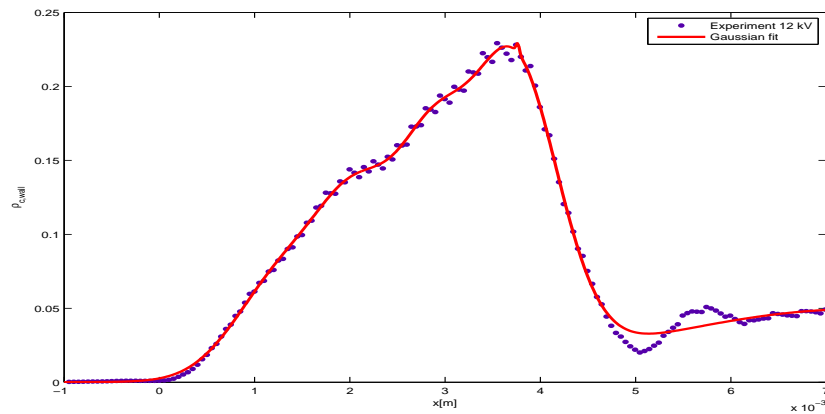


Figure 4.23: Extracted charge density profile on the wall together with a Gaussian fit for $V_{pp} = 12kV$

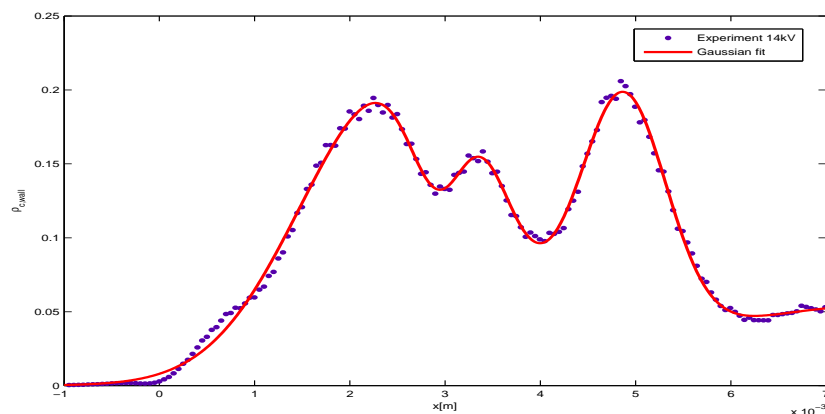


Figure 4.24: Extracted charge density profile on the wall together with a Gaussian fit for $V_{pp} = 14kV$

Helmholtz equation (Equation 4.4). The fact that we obtain a charge density field which is of the same height as the experimental one and where the imposed boundary condition is the same, yet the decay of the charge density field is not the same leads to the conclusion that the charge density

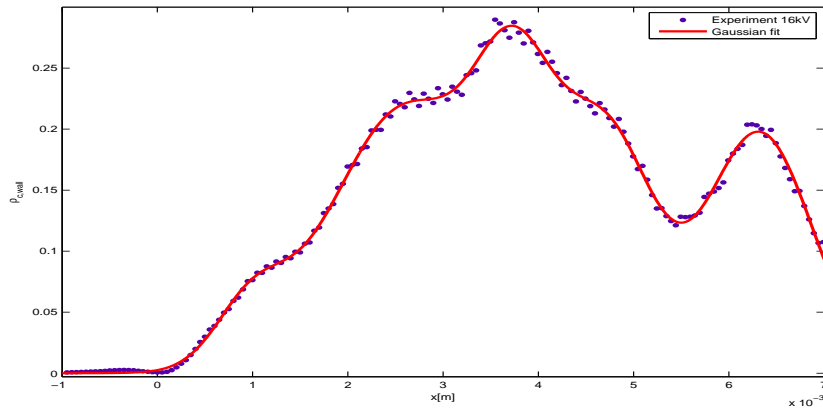
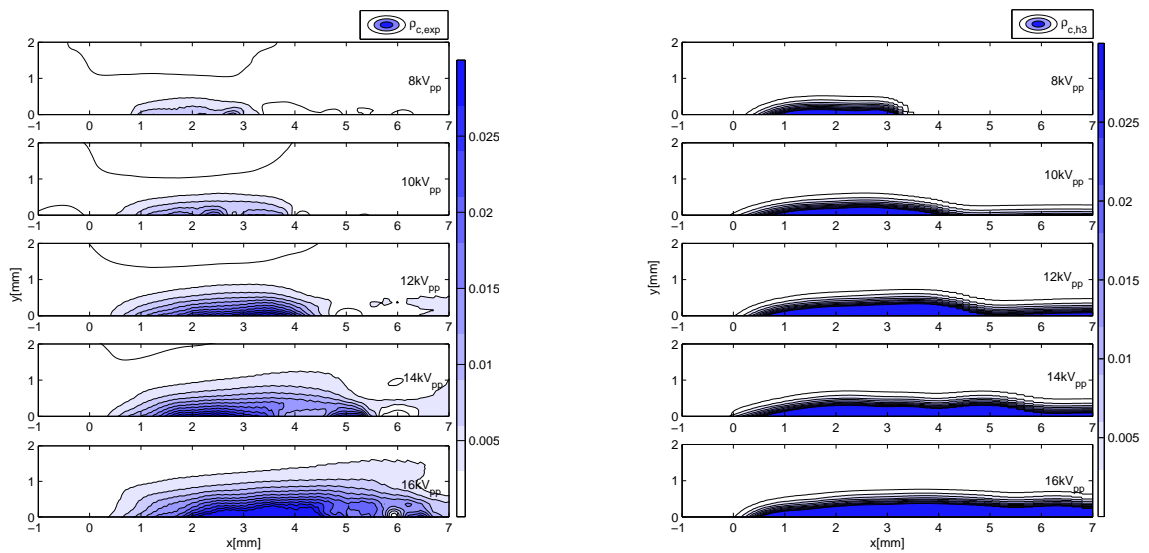


Figure 4.25: Extracted charge density profile on the wall together with a Gaussian fit for $V_{pp} = 16kV$

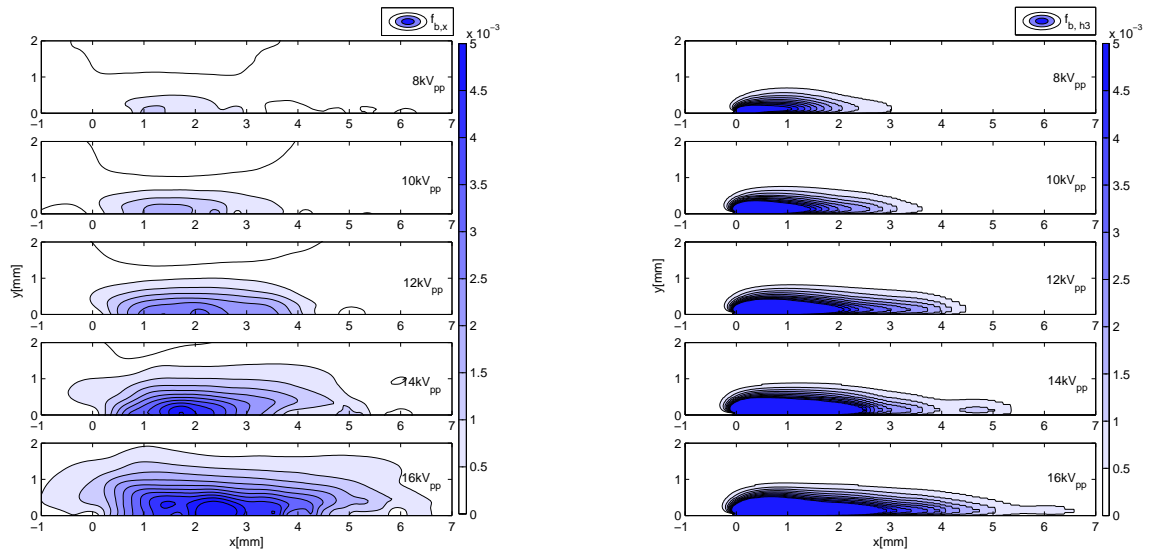
is not modeled correctly or the model of Suzen & Huang is incomplete.



(a) Charge density field extracted from experimental measurements

(b) Modeled charge density field using Hypothesis 3

Figure 4.26: Comparison of experimental and modeled charge density fields for Hypothesis 3



(a) Horizontal body force field extracted from experimental measurements

(b) Modeled body force field using Hypothesis 3

Figure 4.27: Comparison of experimental and modeled body force fields for Hypothesis 3

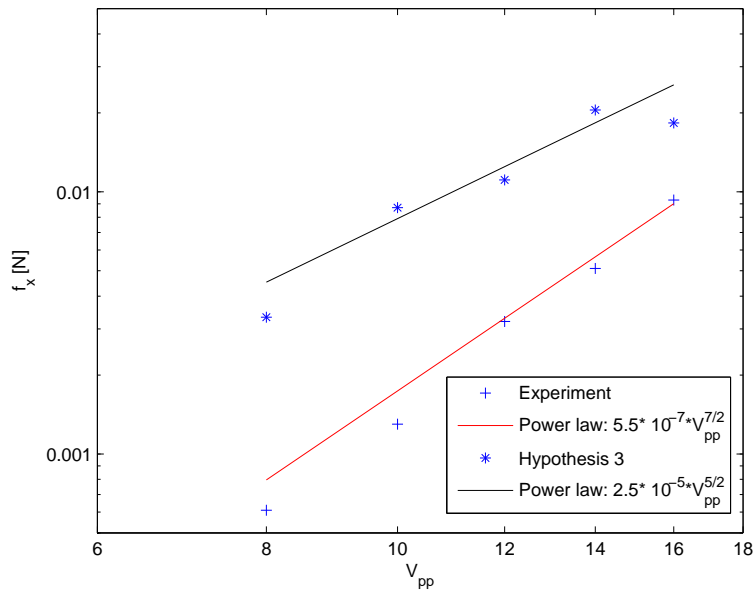


Figure 4.28: Integrated horizontal body force f_x for various voltages using Hypothesis 3

4.8 Analysis of the model of Suzen & Huang

The previous hypotheses showed that the model of Suzen & Huang is not able to model the charge density field in a correct manner. Now let us re-analyze the derivation of the model of Suzen & Huang and use approximation symbols where they are relevant. Let us jump in, in the derivation at the equation for the net charge density field given by:

$$\nabla \cdot (\varepsilon_r \nabla \varphi) = -\frac{\rho_c}{\varepsilon_0} \quad (4.3)$$

After some derivation steps we find the Helmholtz equation for the net charge density:

$$\nabla \cdot (\varepsilon_r \nabla \rho_c) \approx \frac{\rho_c}{\lambda_d^2} \quad (4.4)$$

If we look at the equations, we go from an exact solution (Equation 4.3) to an approximate equation (Equation 4.4). This, because we use the relation:

$$\rho_c \approx -\frac{\varepsilon_0}{\lambda_d^2} \varphi \quad (4.5)$$

This relation is based on a Taylor expansion of the exact relation for $\varphi \ll T$:

$$\frac{\rho_c}{\varepsilon_0} = \frac{e(n_i - n_e)}{\varepsilon_0} = -e \frac{n_0}{\varepsilon_0} \left[\exp\left(\frac{e\varphi}{kT_i}\right) + \exp\left(\frac{e\varphi}{kT_e}\right) \right] \quad (4.6)$$

which becomes:

$$\frac{\rho_c}{\varepsilon_0} \approx -e \frac{n_0}{\varepsilon_0} \left[\left(\frac{e\varphi}{kT_i}\right) + \left(\frac{e\varphi}{kT_e}\right) \right] = -\frac{\varphi}{\lambda_d^2} \quad (4.7)$$

We found in Hypothesis 3 that the model of Suzen & Huang, is inaccurate in the representation of the decay rate of the charge density even though the correct boundary conditions are applied. A reason for this could be that the approximation of Equation 4.7 is inaccurate. Equation 4.7 is based on the assumption that $\varphi \ll T$. This assumption could be the source of inaccuracy of the model. In literature however, it is described that this assumption is questionable [21].

Improvement of the model can be reached by decomposition of the net charge density ρ_c in the species n_i and n_e . This is a more fundamental description of the net charge density ρ_c . With this decomposition, research can be focused on (phenomenological) modeling of the separate species n_i and n_e to obtain a more accurate charge density field.

4.9 Limitations and usage of the model of Suzen & Huang

With calibration of λ_d and $\rho_{c,max}$, the model of Suzen & Huang demonstrated that it is able to induce qualitatively the correct flow stream in the surrounding air. Furthermore, the magnitude of the induced jet stream is physical with respect to experimental data. Therefore, the model could be used for steady flows and separation control purposes.

In the current chapter however, we have demonstrated that the net charge density distribution and therefore the body force distribution obtained from the model of Suzen & Huang are not accurate. Attempts to generalize the model have failed due to the fundamental description of the model. This tells us that calibration for every configuration is needed in order to use the model with a different configuration than the one used in the works of Suzen & Huang.

We can conclude that the model is reasonably accurate, with calibration of the mentioned parameters, when one is interested in the time-averaged effect of the body force on the flow field. The model is based on an electrostatic formulation. The model produces a time-averaged body force field resulting from a complete AC cycle. This makes the model inaccurate in the time-variation of the body force during an AC cycle. In unsteady flow problems, we are more interested in the body force field during the AC voltage cycle. An example of this is the usage of the plasma actuator for transition delay by means of Tollmien-Schlichting wave cancellation. In this case one is in need of the time-dependent body force field during an AC cycle and the change of this body force for changing AC voltages. The Suzen & Huang model can not be used for this purpose due to its time-independency.

Conclusions and Next steps

5.1 Conclusions

The research in different plasma actuator models resulted in two groups of plasma actuator models: Simplified models and First-principles based models. Although the First-principles based models are more accurate than simplified models, they are more complex and therefore computationally intensive. Because this is the first attempt at Delft University of Technology for the implementation of a plasma actuator model, simplicity is an essential starting point. The model of Suzen & Huang is simple, fast and easy to implement. The implementation is done in the commercial CFD-software Fluent, by using the User-Defined Scalar transport equations (UDS). Two separate UDSs are computed: one for the electric potential ϕ and one for the net charge density ρ_c . The code is verified by means of the Method of Manufactured Solutions. The UDS transport equations showed to have second order accuracy.

The code is validated by comparison with the results obtained by Suzen & Huang. The electric potential field, net charge density field and the corresponding body force field showed although with minor differences, to be accurately modeled. The resulting flow field in quiescent air was qualitatively correct, however differences were found in the results obtained by Suzen & Huang and the results of the current simulation. The reason for this could lie in the fact that in the works of Suzen & Huang no information is given regarding the used domain and grid.

Finally, an attempt is made to generalize the model of Suzen & Huang and to analyze its capability of accurately modeling experimentally obtained body force field for a different plasma actuator configuration. The measurements of Kotsonis et al are used as a benchmark and the net charge density field is extracted from the body force measurements by division by the electric field strength. We found that even though the correct boundary conditions are applied, the model of Suzen & Huang is not able to accurately model the charge density field and body force field. A reason for this could be the assumption in the derivation of the model that $\varphi \ll T$. In literature, it is described that this assumption is questionable [21].

Furthermore, the model is not able to compute the change in plasma volume as a function of the applied voltage. The relation between the integrated horizontal body force and the applied voltage is not the relation of $U_{max} \propto f_{b,x} \propto V_{pp}^{7/2}$ found in literature. Therefore, usage of the plasma actuator model for different voltages will introduce an inaccuracy in the magnitude of the integrated horizontal body force and therefore in the maximum induced velocity.

We can conclude that the model is reasonably accurate, with calibration of the mentioned parameters, when one is interested in the time-averaged affect of the body force on the flow field. The model is based on an electrostatic formulation, which makes the model inaccurate in the time-variation of the body force during an AC cycle. This makes the model inaccurate for usage of unsteady flow problems such as transition delay. However, the model could be useful when modeling steady flows and using it for separation control purposes. After calibration, the model could be used in different actuator configurations.

5.2 Next steps

For future work, there are two fields of research that could be useful for the successful implementation of a widely usable plasma actuator model for Delft University of Technology. The first field of research focuses on the improvement of the used Suzen & Huang model. The second field of research is the implementation of a new and more advanced plasma actuator model.

1. In Hypothesis 3 of Chapter 4, we found that the Helmholtz equation for the net charge density is simply inaccurate to represent the charge density field. A way of improvement of the model of Suzen & Huang can be reached by decomposition of the net charge density ρ_c in the species n_i and n_e . With this decomposition, research can be focused on (phenomenological modeling) of the separate species n_i and n_e to obtain a more accurate charge density field without entering the field of First-principles based models. Furthermore, no use is made of the questionable assumption that $\varphi \ll T$. A decomposition could result in two extra differential equations for the calculation of the species n_i and n_e . A potential drawback of this approach is a computationally slower plasma actuator model due to the introduced equations.
2. In the search for a more widely usable plasma actuator model, one could research the implementation of the Lumped element circuit model. This model, developed by Orlov & Corke, is accurate in the modeling of the relation of the maximum induced velocity as a function of the applied voltage $U_{max} \propto f_{b,x} \propto V_{pp}^{7/2}$. Furthermore, the model is time-dependent and therefore has the ability to model the separate half cycles of the plasma actuator. The model showed to be accurate in the modeling of the plasma extent as a function of the input voltage [19]. All this will prove of value when modeling usage of the actuator for unsteady aerodynamic phenomena control such us transition delay. The model uses five equations for the calculation of the extent of the plasma as a function of time and therefore the model will be computationally more intensive than the model of Suzen & Huang. Especially for more advanced plasma actuator applications, this field of research will be valuable.

Bibliography

- [1] P.H. Belenguer and J.P. Boeuf. Transition between different regimes of rf glow discharges. *Phys Rev A*, 1990.
- [2] G.A. Bird. Monte carlo simulations of gas flows. *Ann. Rev. Fluid Mech.* 1978. 10: 11-31, 1978.
- [3] Francis F. Chen. *Introduction to Plasma Physics and Controlled Fusion Plasma Physics*. 1974.
- [4] Thomas C. Corke, C. Lon Enloe, and Stephen P. Wilkinson. *Annual Review of Fluid Mechanics*, 42.
- [5] C. L. Enloe, Thomas E. McLaughlin, Robert D. VanDyken, and John C. Fischer. Mechanisms and responses of a single dielectric barrier plasma actuator: Geometric effects. *42nd AIAA Aerospace Sciences Meeting and Exhibit*, 2004.
- [6] C.L. Enloe, T.E. McLaughlin, R.D. VanDyken, and K.D. Kachner. Plasma structure in the aerodynamic plasma actuator. *AIAA Journal*, 2004.
- [7] A. Fiala, L.C. Pitchford, and J.P. Boeuf. Two-dimensional hybrid model of low-pressure glow discharges. *Phys Rev E*, 1994.
- [8] M. Forte, J. Jolibois, J. Pons, E. Moreau, G. Touchard, and M. Cazalens. Optimization of a dielectric barrier discharge actuator by stationary and non-stationary measurements of the induced flow velocity: application to airflow control. *Exp Fluids*, 2007.
- [9] Mohamed Gad-El-Hak. *Flow Control: Passive, Active, and Reactive Flow Management*. 2000.
- [10] S. Grundmann and C. Tropea. *Exp Fluids*, 44.
- [11] K.D. Hall, E.J. Jumper, and T.C. Corke. Potential flow model of a plasma actuator as a lift enhancement device. *43rd AIAA Aerospace Sciences Meeting and Exhibit*, 2005.
- [12] J.D. Jacob, K. Ramakumar, R. Anthony, and R.B. Rivir. Control of laminar and turbulent shear flows using plasma actuators. *Fourth International Symposium on Turbulence and Shear Flow Phenomena*, 2005.
- [13] B. Jayaraman and W. Shyy. Modeling of dielectric barrier discharge-induced fluid dynamics and heat transfer. *Progress in Aerospace Sciences*, 44:139–191, 2008.

- [14] M. Kotsonis, P. Boon, and L. Veldhuis. Plasmas for transition delay. *10th International Conference on Fluid Control, Measurements and Visualization*, 2009.
- [15] M. Kotsonis, S. Ghaemi, L. Veldhuis, and F. Scarano. Measurement of the body force field of plasma actuators. *J. Phys. D: Appl. Phys.*, 2010.
- [16] Alexandre V. Likhanskii, Mikhail N. Shneider, Dmitry F. Opaitis, and Richard B. Miles. *AIAA Plasma dynamics and Lasers Conference*, 38.
- [17] E. Moreau. Airflow control by non-thermal plasma actuators. *J. Phys. D: Appl. Phys.* 40 (2007) 605-636, 2007.
- [18] D.M. Orlov and T.C. Corke. Numerical simulation of aerodynamic plasma actuator effects. *AIAA Aerospace Sciences Meeting and Exhibit*, pages 139–191, 2005.
- [19] D.M. Orlov and T.C. Corke. Electric circuit model for aerodynamic plasma actuator. *AIAA Aerospace Sciences Meeting and Exhibit*, 44, 2006.
- [20] P.J. Roache. Code verification by the method of manufactured solutions. *J. Fluids Eng*, 2002.
- [21] J. Reece Roth. *Industrial Plasma Engineering Volume 1: Principles*. 1995.
- [22] David T. Sandwell. Biharmonic spline interpolation of geos-3 and seasat altimeter data. *Geophysical Research Letters*, 2, 139-142, 1987.
- [23] A. Yu Starikovskii¹, A. A. Nikipelov, M. M. Nudnova¹, and D. V. Roupasov. *Plasma Sources Sci. Technology*, 18.
- [24] M. Surendra and D.B. Graves. Particle simulations of radio-frequency glow discharges. *IEEE Trans Plasma Sci*, 1991.
- [25] Y.B. Suzen and P.G. Huang. Simulations of flow separation control using plasma actuators. *44th AIAA Aerospace Sciences Meeting and Exhibit*, 2006.

Appendix A

User-Defined Functions implemented in Fluent

```
%%%%%%%%%%%%%%%%%%%%%%%%%%%%%%%%%%%%%%%%%%%%%%%%%%%%%%%%%%%%%%%%%%%%%%%%%  
%% DEFINITION OF CONSTANTS %%  
%%%%%%%%%%%%%%%%%%%%%%%%%%%%%%%%%%%%%%%%%%%%%%%%%%%%%%%%%%%%%%%%%%%%%%%%%
```

```
#include "udf.h"  
#include "math.h"  
#include "sg_udms.h"  
#define debye 0.001  
#define rhomax 0.0008  
#define phimax 5000  
#define sigma 0.003  
#define rholoc 0.5
```

```
enum {  
phi,  
rho  
};
```

```
enum {  
Ex,  
Ey,  
Fx,  
Fy,  
Fm  
};
```

```
%%%%%%%%%%%%%%%%%%%%%%%%%%%%%%%%%%%%%%%%%%%%%%%%%%%%%%%%%%%%%%%%%%%%%%%%%  
%% CALCULATION OF ELECTRIC FIELD STRENGTH %%  
%%%%%%%%%%%%%%%%%%%%%%%%%%%%%%%%%%%%%%%%%%%%%%%%%%%%%%%%%%%%%%%%%%%%%%%%%
```

```

DEFINE_ADJUST(udf_adjust, domain)
{
  Thread *t;
  cell_t c;

  thread_loop_c(t, domain)
  {
    begin_c_loop(c, t)
    {

      C_UDMI(c, t, Ex) = -C_UDSI_G(c, t, phi) [0];
      C_UDMI(c, t, Ey) = -C_UDSI_G(c, t, phi) [1];

    }
    end_c_loop(c, t)
  }
}

%%%%%%%%%%%%%%%%%%%%%%%%%%%%%%%%%%%%%%%%%%%%%%%%%%%%%%%%%%%%%%%%%%%%%%%%
%% DEFINITION OF SOURCE OF HELMHOLTZ EQUATION %%
%%%%%%%%%%%%%%%%%%%%%%%%%%%%%%%%%%%%%%%%%%%%%%%%%%%%%%%%%%%%%%%%%%%%%%%%

DEFINE_SOURCE(rho_source, c, t, dS, eqn)
{
  real source;

  source = -pow(debye, -2) * C_UDSI(c, t, rho);
  dS[eqn] = -pow(debye, -2);
  return source;
}

%%%%%%%%%%%%%%%%%%%%%%%%%%%%%%%%%%%%%%%%%%%%%%%%%%%%%%%%%%%%%%%%%%%%%%%%
%% DEFINITION OF X-MOMENTUM SOURCE TERM %%
%%%%%%%%%%%%%%%%%%%%%%%%%%%%%%%%%%%%%%%%%%%%%%%%%%%%%%%%%%%%%%%%%%%%%%%%

DEFINE_SOURCE(X_Source, c, t, dS, eqn)
{
  real SourceX;

  SourceX = -rhomax * phimax * C_UDSI(c, t, rho) * C_UDSI_G(c, t, phi) [0];
  dS[eqn] = -rhomax * phimax;

  C_UDMI(c, t, Fx) = SourceX;

  return SourceX;
}

```

```

}

%%%%%%%%%%%%%%%%%%%%%%%%%%%%%%%%%%%%%%%%%%%%%%%%%%%%%%%%%%%%%%%%%%%%%%%%
%% DEFINITION OF Y-MOMENTUM SOURCE TERM %%
%%%%%%%%%%%%%%%%%%%%%%%%%%%%%%%%%%%%%%%%%%%%%%%%%%%%%%%%%%%%%%%%%%%%%%%%

DEFINE_SOURCE(Y_Source, c, t, dS, eqn)
{
  real Sourcey;

  Sourcey=-rhomax*phimax*C_UDSI(c,t,rho)*C_UDSI_G(c,t,phi)[1];
  dS[eqn]=-rhomax*phimax;

  C_UDMI(c,t,Fy)=Sourcey;
  C_UDMI(c,t,Fm)=sqrt(C_UDMI(c,t,Fx)*C_UDMI(c,t,Fx)+C_UDMI(c,t,Fy)*C_UDMI(c,t,Fy));
  return Sourcey;
}

%%%%%%%%%%%%%%%%%%%%%%%%%%%%%%%%%%%%%%%%%%%%%%%%%%%%%%%%%%%%%%%%%%%%%%%%
%% DISTRIBUTION FUNCTION ON WALL %%
%%%%%%%%%%%%%%%%%%%%%%%%%%%%%%%%%%%%%%%%%%%%%%%%%%%%%%%%%%%%%%%%%%%%%%%%

DEFINE_PROFILE(rho_profile,thread,i)
{
  float r[3];
  float x;
  real xloc;
  face_t f;

  begin_f_loop(f,thread)
  {
    F_CENTROID(r,f,thread);
    xloc = r[0];

    F_PROFILE(f,thread,i)=exp(-pow((xloc-rholoc),2)/(2*pow(sigma,2)));
  }
  end_f_loop(f,thread)
}

```

Appendix B

Gaussian coefficients for Hypothesis 3

Coefficients	8kV	10kV	12kV	14kV	16kV
A_1	0.06791	-0.2658	0.006303	0.1636	0.2179
B_1	0.002815	0.003071	0.003763	0.004872	0.00262
C_1	0.0003684	0.0005886	$2.477 \cdot 10^{-5}$	0.0006389	0.001138
A_2	0.02007	0.3377	32.97	0.05537	0.1699
B_2	0.00196	0.003046	0.003056	0.007885	0.003751
C_2	0.0003182	0.0006639	0.0007601	0.003703	0.0005794
A_3	-0.0004361	0	-32.55	0.1927	0.04901
B_3	0.00149	0.002825	0.003062	0.002414	0.0009885
C_3	$4.399 \cdot 10^{-5}$	$1.843 \cdot 10^{-6}$	0.0007525	0.001338	0.0005278
A_4	0.02454	-0.001633	0.04944	0.08213	0.1923
B_4	0.002272	0.002116	0.007347	0.003212	0.004703
C_4	0.0002269	$6.062 \cdot 10^{-5}$	0.003207	0.000482	0.0007196
A_5	0.00599	0.07388	-0.53	-0.103	0.1966
B_5	0.002491	0.001689	0.002528	0.00299	0.00632
C_5	0.0001116	0.0009745	0.000588	0.0004352	0.0007877
A_6	0.06409	0.0161	0.06871	0	0
B_6	0.001464	0.006593	0.001309	0	0
C_6	0.0007042	0.003778	0.0007131	0	0

Table B.1: Coefficients used for Gaussian curve fit Hypothesis 3

